

Fighting the curse of dimensionality: A machine learning approach to finding global optima

Julian F. Schumann,¹ Alejandro M. Aragón^{1*}

¹Department Precision and Microsystems Engineering, Technological University Delft,
Mekelweg 2, 2628 CD Delft, Netherlands

*To whom correspondence should be addressed; E-mail: a.m.aragon@tudelft.nl

Finding global optima in high-dimensional optimization problems is extremely challenging since the number of function evaluations required to sufficiently explore the design space increases exponentially with its dimensionality. Furthermore, non-convex cost functions render local gradient-based search techniques ineffective. To overcome these difficulties, here we demonstrate the use of machine learning to find global minima, whereby autoencoders are used to drastically reduce the search space dimensionality, and optima are found by surveying the lower-dimensional latent spaces. The methodology is tested on benchmark functions and on a structural optimization problem, where we show that by exploiting the behavior of certain cost functions we either obtain the global optimum at best or obtain superior results at worst when compared to established optimization procedures.

Introduction

Ever since Newton minimized the resistance of a radial symmetric body in a fluid flow (1), countless optimization problems have occupied the minds of scholars. Today, as humanity struggles with an ever-increasing population and a finite amount of resources (2), optimization plays a fundamental role in enabling greater efficiency in the use of materials and energy (3, 4, 5, 6). The advent of computers and the increase in computational power over the years (7) has also enabled the solution of increasingly complex optimization problems in numerous fields such as

engineering, medicine, and economics (8, 9, 10). Still, the optimization of high-dimensional problems that are characterized by a non-convex cost function—where the global optimum sought is one of many local optima—still poses significant challenges. This is caused by the so-called “curse of dimensionality,” whereby the number of cost function evaluations required for a sufficiently thorough survey of the search space increases exponentially with the number of dimensions (11, 12). This becomes even more troublesome for computationally-intensive problems, where the cost of function evaluations further limits the size and consequently the dimensionality of the space that can be explored.

A plethora of algorithms have been proposed over the years to optimize high-dimensional problems (13, 14). They are, however, all limited by the so-called “no free lunch theorem,” whereby optimization algorithms theoretically perform the same when averaged over all possible optimization problems (15, 16). As a result, a certain algorithm can only be more efficient than others on a certain set of optimization problems, where it is best at exploiting a common property of these problems’ cost functions. For example, gradient-based algorithms are superior on convex, differentiable cost functions, but often are unable to find global optima on non-convex cost functions. When trying to overcome this limitation and improve over gradient-based search, one usually turns towards global optimization algorithms,¹ for instance surrogate model-based Bayesian optimization or metaheuristic search (19). On the one hand, Bayesian optimization was *designed* for problems with expensive cost function evaluations (17), but struggles with high-dimensional search spaces, with recent works considering problems with at most a few hundred dimensions (20, 21). This is because the construction of the surrogate model, which requires the repeated inversion of a dense, often ill-conditioned (near singular), and large matrix (19)—with size proportional to the dimensionality of the problem (17)—is not only time-consuming but can also lead to memory issues (22). On the other hand, metaheuristic search algorithms can be used for high-dimensional problems, but are only applicable to relatively inexpensive cost functions due to the vast number of function evaluations required. Population-based search algorithms like genetic algorithms (23), differential evolution (18), or particle swarm optimization (24) are widely used examples of heuristic search methods.

¹Here *global* does not imply surveying the entire space, but just different portions of it in a way that the search can escape local optima basins (17, 18).

In this work we focus on problems where large portions of the search space can be discarded. Model order reduction (MOR) can then be used to limit the search space to regions where the global optimum is likely to be found. To that end, we use autoencoders—which especially for non-linear MOR have been shown to be superior to other methods such as proper orthogonal decomposition (POD) (25, 26, 27, 28, 29, 30)—to obtain a *latent space* with drastically reduced dimension; autoencoders use two feed-forward neural networks that learn to copy the input to the output: The encoder network maps the input into the lower-dimensional latent space, and the decoder network is trained to reconstruct the input (31). Once an autoencoder is trained, global optimization over the latent space then becomes feasible. Since global optimization over lower-dimensional spaces is covered extensively in the literature, be it by heuristic search for inexpensive cost functions (32, 33, 34, 35) or Bayesian optimization for comparatively expensive cost functions (17, 36, 37), the main focus of this work is on autoencoders.

The use of autoencoders to enable global optimization in latent spaces was first studied by Costa in a constrained wind-hydro coordination problem (38), although it was only applied to a relatively low-dimensional problem (120 dimensions with a reduction in dimensionality by only a factor of 2). A similar work was also pursued by Miranda *et al.* (39), who also used this method to achieve faster convergence on a number of benchmark functions. Gao *et al.* applied autoencoders to fit a geology model to data, reducing the dimensionality from 38 400 dimensions down to 140 (40, 41). Eismann *et al.* (42) used an autoencoder in a fluid resistance minimization problem, reducing the 9408-dimensional problem to a 20-dimensional latent space. They also added a neural network-based surrogate model that mapped a latent space sample to a scalar value. Training this network and the autoencoder simultaneously, so that the surrogate network’s output approximates the cost function value of the high-dimensional encoder input, led to a latent space with more evenly spaced local optima and more moderate gradients; this was beneficial for using Bayesian optimization over the latent space. Although improved designs for the drag minimization problem were obtained, the procedure used is flawed because training samples for the autoencoder were generated randomly and therefore its effectiveness is limited, since the training samples have no inherent features the autoencoder could learn. Meanwhile, Kudyshev *et al.* proposed the use of an adversarial autoencoder to enforce a certain distribution of designs in latent space when optimizing phononic metamaterials (43). Autoen-

coders for reducing the search space have also been employed in other works, for example in the design of electromagnetic circuits (44, 45), optical microstructures (46), mechanical structures such as springs (47) or wheels (48), and even for designing molecules (49).

While the aforementioned works already use autoencoders to reduce the dimensionality of an optimization problem, there is lack of justification for their successful application in regard to the “no free lunch theorem”—besides reporting improved designs. For example, none of the aforementioned works explains why their training data has a lower intrinsic dimensionality which the autoencoder might exploit, and some even use completely random training samples (42). Furthermore, the authors do not explain why their proposed methods should still be able to find global optima reliably despite the reduction in dimensionality, which makes the use of autoencoders for global optimization algorithms questionable at best. Consequently, it is also unclear for what kind of other optimization problems this approach could be used.

Exploring sufficiently the search space in pursuit of a global optimum is limited by two main factors, namely the dimensionality n of the search space and the time required for a single cost function evaluation t_c . In this work we propose a generalized framework for autoencoder enabled global optimization that addresses the former, enabling a significantly faster convergence on some specific optimization problems, where the objective is to solve

$$\mathbf{x}_{\min} = \underset{\mathbf{x} \in X}{\operatorname{argmin}} c(\mathbf{x}), \quad X \subset \mathbb{R}^n \quad (1)$$

in a limited amount of time. To find the global minimum \mathbf{x}_{\min} , we assume that a lower-dimensional manifold $X_Z \subset X \subset \mathbb{R}^n$ —which is the *decoded latent space* of an autoencoder trained on a number of sampled local minima; the latter are found by randomly sampling the high-dimensional search space X and subsequent local gradient-based search—goes through the basin X_{\min} of the global optimum. This discards large uninteresting regions of the design space where we assume that the global optimum is unlikely to be found. The procedure is schematically shown in **Fig. 1**, where $c(\mathbf{x})$ is the cost function of the high-dimensional space X (in **Fig. 1A** $X \subset \mathbb{R}^2$ for visualization purposes, but the dimensionality could be arbitrarily high). The encoder component E of the autoencoder (**Fig. 1B**) maps a point $\mathbf{x} \in X$ to a lower-dimensional point $E(\mathbf{x}) = \mathbf{z} \in Z$ (**Fig. 1C**, where $\mathbf{z} \in \mathbb{R}$). The decoder component D (**Fig. 1D**) then maps such latent space samples back into the high-dimensional space, *i.e.*,

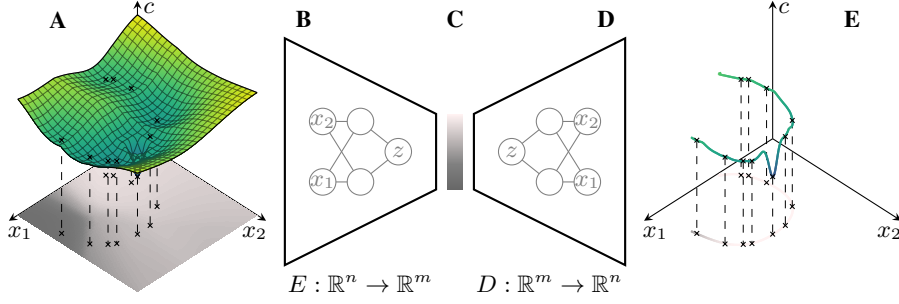


Fig. 1: Visualization of the underlying idea. Instead of optimizing over the whole domain $X \subset \mathbb{R}^n$ (**A**), an autoencoder is trained first. Here the encoder E (**B**, the grayscale coding in **A** and **C** is used to represent this function) maps a sample x from the design space into the latent space $Z \subset \mathbb{R}^m$ (**C**). A decoder D (**D**, the same grayscale coding is used, here in **C** and **E**) then transforms the latent space sample z back into higher-dimensional domain X , although the decoded samples will be part of the lower dimensional manifold $X_Z \subset X$ (**E**), over which the global optimization is then performed.

$D(z) \in X_Z$ (**Fig. 1E**). The specific X_Z is then the result of the autoencoder training, where the autoencoder tries to minimize the error between the input sampled local minima (see \times markers on $c(x)$ in **Fig. 1A**) and their reconstructed counterparts. This proposed method is then viable if the latent space dimensionality m is larger than or equal to the intrinsic dimensionality m^* of the optimization problem—which can be understood as the number of features distinguishing usable regions of the design space (see Appendix 3.1)—and if m^* is significantly smaller than n , then optimizing over $Z \subset \mathbb{R}^m$ would require significantly fewer cost function evaluations than optimizing over $X \subset \mathbb{R}^n$. The procedure is described in more detail in § **Methods**. It is worth mentioning that this method is only useful if random multi-start local search (50) is unable to find the global optimum, which is the method we use to generate the autoencoder’s input data. Only then the optimization over latent space and the associated exploration of other promising regions of the high-dimensional search space could be effective, as the autoencoder is able to generate a decoded latent space X_Z going through the basin of the global minimum even when trained with no samples in such basin.

Results

The methodology is tested on constructed benchmark functions and on a real-world compliance minimization problem.

Benchmark functions

We first test the procedure on the following cost function:

$$c_1(\mathbf{x}) = \min_i \|\mathbf{x} - \mathbf{x}_i\|^2 + 3 \left(1 - \exp\left(-10 \|\mathbf{x} - \mathbf{x}_1\|^2\right)\right) \left(\frac{2}{5} + \exp\left(-10 \|\mathbf{x} - \mathbf{x}_1\|^2\right)\right). \quad (2)$$

This function was designed specifically to have an intrinsic dimensionality $m^* = 10$ (see Appendix 3.3), with $\mathbf{x}_i \in \{\mathbf{x}_1, \dots, \mathbf{x}_{2500}\} = \mathbf{X}$ being 2500 points arrayed on a 10-dimensional manifold in the $n = 1000$ dimensional design space $X_1 = [-1, 1]^n$. We then used our proposed approach to minimize c_1 with latent spaces of dimensions $m = \{5, 10\}$, and also compare our results with those obtained by differential evolution. For details of the creation of \mathbf{X} and the implementation of the optimization see Appendix 2.1.

The procedure is also tested on other cost functions borrowed from the work of Abualigah *et al.* (51):

$$\begin{aligned} c_2(\mathbf{x}) &= \sum_{i=1}^n \left(-x_i \sin\left(\sqrt{|x_i|}\right)\right) + 418.9829n \\ c_3(\mathbf{x}) &= \frac{\pi}{n} \left(10 \sin(\pi y(x_1))^2 + \sum_{i=1}^{n-1} (y(x_i) - 1)^2 \left(1 + 10 \sin(\pi y(x_{i+1}))^2 + u(\mathbf{x})\right)\right) \\ y(x) &= \frac{x + 5}{4}, \quad u(\mathbf{x}) = \sum_{i=1}^n 100 \max\{0, |x_i| - 10\}^4 \\ c_4(\mathbf{x}) &= 1 + \frac{1}{4000} \sum_{i=1}^n (x_i^2) - \prod_{i=1}^n \left(\cos\left(\frac{x_i}{\sqrt{i}}\right)\right) \end{aligned} \quad (3)$$

All of these three functions are minimized over an $n = 100$ dimensional domain, with $X_2 = X_4 = [-500, 500]^n$ and $X_3 = [-50, 50]^n$. For this, the proposed method is using autencoders with a latent space dimensionality of $m = 5$, and for c_3 and c_4 , also autoencoders with $m = 2$. The exact implementation of the optimization process can be seen in Appendix 2.2. All four functions in this section have a global minimum $c_i = 0$.

Noteworthy, as these three functions' local minima are spread roughly evenly over the whole domain X_i , one can expect that the intrinsic dimensionality of the problem $m^* = n = 100$, as there are no features in the training sample an autoencoder could learn. If this is indeed the case, the proposed method with $m \leq 5$ will most likely not find the global optimum.

Fig. 2 summarizes the results, where for each of the optimization runs, the lowest found cost function value after a certain number of cost function evaluations n_F is shown; this is done for each of the steps of the proposed method, *i.e.*, the generation of the autoencoder training

samples (solid lines), the optimization over latent space (dashed lines), and finally the post processing (dotted lines) (see § **Methods**). But the minimum values found in a given step of the method are ignored in the subsequent step to better discriminate between them.

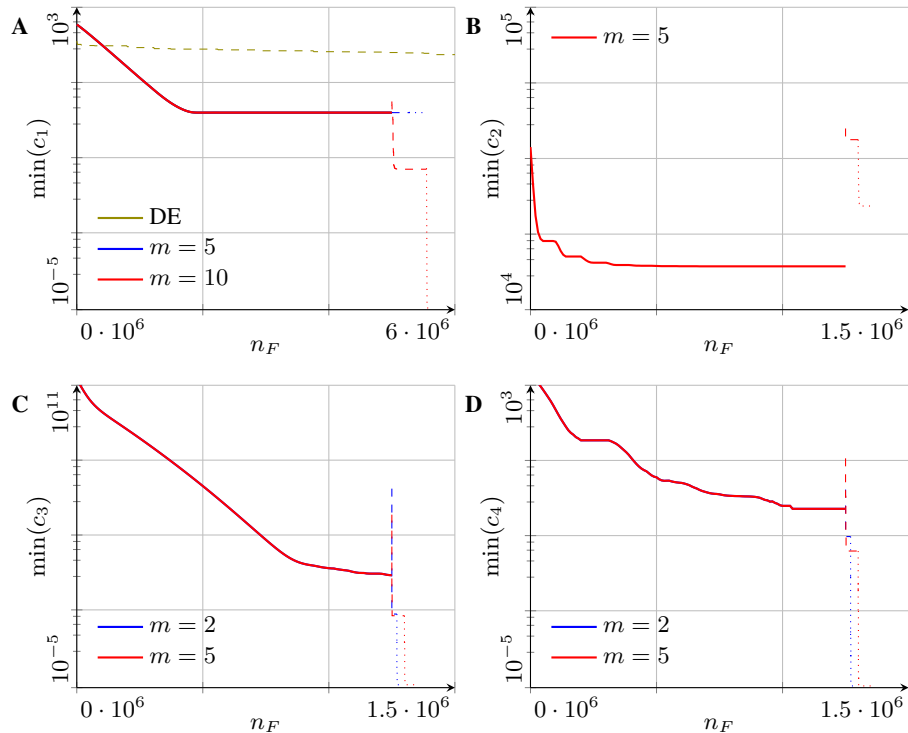


Fig. 2: The results of optimizing the functions c_1 (**A**), c_2 (**B**), c_3 (**C**), and c_4 (**D**). The continuous lines describe the first step, where λ steps of local optimization are used on 10 000 random initial points. The dashed lines show the minimum during the optimization over latent space, while the dotted lines show the best cost function during post-processing. For cost function c_1 , one can also see the results of using differential evolution in the high-dimensional search space in olive.

It can be seen in **Fig. 2A** that the global optimum of c_1 can only be found with the proposed method with $m = 10$, while both the proposed method with $m = 5$ as well as standard differential evolution are unsuccessful. These results are as expected, since the function was designed so that $m^* = 10$, which gave the event of finding the global optimum for $m = 5$ a lower probability. A similar expected result could be found in the optimization of c_2 (see **Fig. 2B**), where the optimization was indeed not successful, since $m \ll m^* = n$.

In contrast, the optimization succeeds for c_3 and c_4 in spite of using an autoencoder with $m \ll n$ (see **Figs. 2C** and **2D**, respectively). The reason for this is that contrary to c_2 , the global optimum of these functions lies precisely at the center of an evenly spread cluster of local minima. As is shown in Appendix 3.4, in such cases the intrinsic dimensionality m^* of

the problem might fall as low as $m^* = 1$, and therefore, the proposed method was indeed able to find the global optimum (although there were no parts of the design space we could discard *a priori*).

Compliance minimization

After testing the proposed method on benchmark functions, we turn our attention to a more realistic problem, namely topology optimization. We minimize the compliance C of a beam under a force F subject to a constraint on the amount of solid material that can be used. The rectangular computational domain is subdivided into $n_y \times n_x$ cells or *finite elements*, each of which is assigned a material density $0 \leq x_j \leq 1$. Some void non-design regions are also enforced *a priori*, whose purpose is to increase the non-convexity of the problem. This would allow for a better assessment of the proposed method in comparison to the standard gradient-based approach that is normally used for such problems (see **Fig. 3A** for a visualization of the problem and Equation (53) for a mathematical description).

The problem is solved on a finite mesh composed of $n_y \times n_x = 45 \times 90$ finite elements, and an autoencoder with $m = 100$ dimensions is chosen. This autoencoder uses a novel architecture, namely an adversarial autoencoder which also benefits from using a surrogate neural network during training (see Appendix 1.3), which was selected by comparing differing architectures. Furthermore, instead of encoding the density field \mathbf{x} , one uses a quasi signed distance field ψ (see Appendix 1.5), which is also a novel approach in the field of autoencoder enabled global optimization. We then search the latent space by means of two procedures, namely the heuristic search provided by differential evolution and also Bayesian optimization. The results from these two procedures are also compared to those obtained by standard topology optimization, for which gradient-based local search with an initial homogeneous material distribution is used (52). The actual implementation for this compliance minimization problem can be found in Appendix 2.3.

The structural designs obtained are shown in **Fig. 3**. Standard topology optimization yielded the design in **Fig. 3A** with a compliance $C_{\text{TO}} = 94.86$ (1000 steps of SIMP after an initial design of homogeneous material throughout the computational domain). The best design obtained during training, shown in **Fig. 3B**, achieved a compliance $C_{\text{T}} = 92.65$. Then the search over

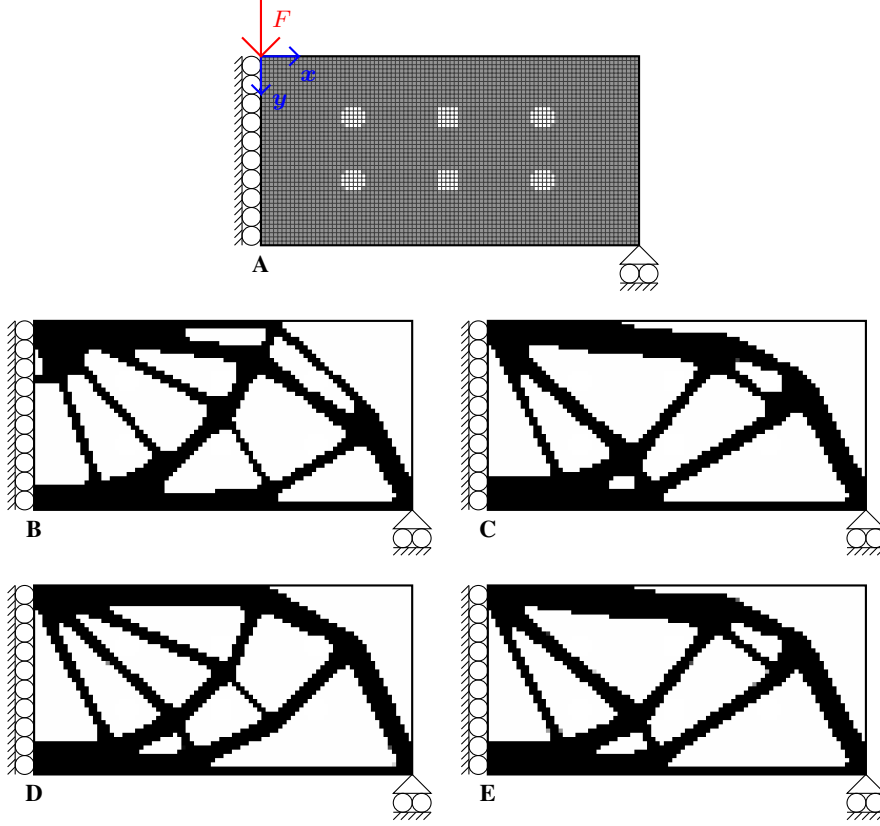


Fig. 3: (A) Schematic of the Messerschmitt-Bölkow-Blohm (MBB) beam problem showing boundary conditions and non-design void regions (white finite elements); (B) design obtained using standard topology optimization (1000 steps of SIMP after an initial homogeneous material distribution), with a compliance $C_{TO} = 94.86$; (C) design with the lowest compliance $C_T = 92.65$ obtained during training (local gradient-based optimization on 5000 initial random configurations); and (D,E) designs obtained using the proposed approach with differential evolution (D) and Bayesian optimization (E) for the latent space search. Compliance values are $C_{DE} = 91.64$ and $C_{BO} = 91.98$ respectively.

latent space yielded designs with a compliance $C_{DE} = 91.64$ and $C_{BO} = 91.98$ for differential evolution and Bayesian optimization, respectively. This shows that the proposed procedure outperforms both standard SIMP and random multi-start local optimization. Still, it cannot be determined if the best compliance found (C_{DE}) corresponds to the global minimum because the original design space is extremely vast; the number of sparse designs ($x_j \in \{0 \text{ or } 1\}, \forall x_j \in \mathbf{x}_i, \forall \mathbf{x}_i \in X_s \subset X$) is extremely large, with $|X_s| \approx 6.5 \times 10^{1172}$ designs. And even if the mass constraint is applied, one still has to content with $\approx 6.7 \times 10^{1146}$ designs, which rules out any use of brute force search. A calculation of these numbers can be found in Appendix 3.5.

Besides the compliance value of final designs, the time required to achieve these also needs to be considered when evaluating the method's performance. As summarized in **Tab. 1**, the

proposed procedure took at least three hours to complete in a parallel environment with 100 processes. Meanwhile, with only one of these cores, generating a design using the standard method with homogeneous input only took five and a half minutes. In **Tab. 1** one can also see that differential evolution for this specific problem is much faster, as the compliance is relatively inexpensive to evaluate (more details in Appendix 3.6). While this might shift in favor of Bayesian optimization for more expensive cost functions (*e.g.*, when using more steps of local optimization during the third step of the proposed method, see § **Methods**), potential time savings come at the expense of reducing the likelihood of finding the best possible design due to the lower number of cost function evaluations for Bayesian optimization—which can be seen for example in this compliance minimization problem.

Tab. 1: The number of cost function evaluations n_F —with one instance of solving the finite element problem being counted of evaluation, so C and LO are counted equally—and the time t that are needed for each step of the proposed method (see § **Methods**). Step 1, the generation of the training samples, uses 50 processor cores, while steps 2 (training the autoencoder) and 3 (optimizing over latent space using differential evolution (DE) or Bayesian optimization (BO)) each have 100 processor cores available. The final step 4, the post-processing, then is done without parallel processing.

Step	1	2	3 - DE	3 - BO	4
n_{ef}	1.6×10^6	0	5.3×10^6	4.6×10^4	3.1×10^2
t (h : min)	1 : 17	0 : 22	1 : 35	14 : 27	0 : 02

Methods

There are two main factors that determine if, and possibly how, an optimization problem

$$\mathbf{x}_{\min} = \operatorname{argmin}_{\mathbf{x} \in X} c(\mathbf{x}), \quad X \subset \mathbb{R}^n \quad (4)$$

can be solved with general optimization methods in a limited amount of time, namely the dimensionality n of the problem and the time t_c it takes to evaluate one instance of the cost function $c(\mathbf{x})$. Optimization problems are solved using an underlying computer architecture that, for a given period of time, imposes an upper bound on the number of possible cost function evaluations, which is approximately inversely proportional to t_c . As the number of cost function evaluations required to sufficiently explore the design space grows exponentially with the number of search variables n (see “curse of dimensionality” (11, 12), although it has to

be noted that some authors seem to assume linear growth to be enough (17), using standard global optimization algorithms becomes unfeasible if the cost function evaluation time and the problem dimensionality are too high.

Since reducing t_c without altering the cost function is usually not possible, optimizing previously unsolvable problems mandates for algorithms that converge with the same likelihood while requiring fewer cost function evaluations. According to the “no free lunch theorem” (15, 16), this is only possible by exploiting the structure of the cost function, which will also limit the range of optimization problems to which this new algorithm can be applied. One way to exploit the problem structure is to build an algorithm that discards large regions of the search space X where the global optimum \mathbf{x}_{\min} is not likely to be found.

Our proposed procedure for global optimization using autoencoders uses sampled local minima to try to construct a lower-dimensional manifold that discards useless regions of the design space and that also contains the global optimum. The procedure comprises the following steps, with an schematic example of them shown in **Fig. 4**.

1. **Generating training samples:** A training set for the autoencoder is generated in a first step, with the goal that the training set features correspond to those of the usable part of the design space. This is done by firstly randomly sampling N points $\mathbf{x}_i \in \mathbb{R}^n$ in the design domain X . Local optimization is then used to advance these points in the direction of their corresponding local minima. \mathbf{X}_λ denotes the set of samples after the λ th step of local optimization, *i.e.*, with LO denoting the local optimization operator (which refers to any local optimization algorithm), $\mathbf{X}_\lambda = \text{LO}[\mathbf{X}_{\lambda-1}] = \text{LO}^\lambda[\mathbf{X}_0]$. The value of λ has to be chosen carefully, since it should be large enough so that training samples \mathbf{X}_λ are useful, and small enough to avoid unnecessary evaluations.

To generate these samples, we use gradient based methods like Adam (53) or alternatively the SIMP method (54) in the case of topology optimization (see Appendix 1.1). But if the cost function is not differentiable ($c(\mathbf{x}) \notin C^1$), zeroth order local optimization methods like the Nelder-Mead algorithm (55) can be used, although for high-dimensional problems this is likely very expensive. It is worth noting that multiple different starting points could yield similar designs after local optimization, undoubtedly wasting computational

resources. To avoid this problem, sampling techniques like deflation could be used (56), whereby new samples are guided away from already explored regions by modifying the cost function.

2. **Training the autoencoder:** In a second step, the samples from X_λ are used to create a latent space of dimensionality m (see Appendix 1.3). While there are different related procedures (autoencoders (57,58), variational autoencoders (VAE) (59), generative adversarial networks (GANs) (60), adversarial autoencoders (AAEs) (61), autoencoder with surrogate model network (42)), this step produces a decoder network $D : \mathbb{R}^m \rightarrow \mathbb{R}^n$, which allows the transformation of sample $z_i \in Z$ out of the latent space $Z \subset \mathbb{R}^m$ into the design space $X \subset \mathbb{R}^n$. Noteworthy, as illustrated earlier in **Fig. 1**, decoded samples $D(z_i)$ occupy an m -dimensional manifold X_Z —the decoded latent space in this work—of the n -dimensional design space ($X_Z = D[Z] \subset X$). Since $D \in C^1$, X_Z will be a continuous domain for a continuous latent space Z .

To have the highest probability of finding the global optimum \mathbf{x}_{\min} , our hope is to construct an autoencoder whose decoded latent space X_Z is as close to the global optimum \mathbf{x}_{\min} as possible, but at least goes through the basin of the global optimum X_{\min} (see Appendix 3.1).

3. **Optimization over latent space:** In this step, by optimizing over latent space, we want to find, as quickly as possible, the closest point to the global minimum. To this end, we minimize the cost function $c_\mu(\mathbf{z})$, *i.e.*,

$$\mathbf{z}_\mu^* = \arg \min_{\mathbf{z} \in Z} c_\mu(\mathbf{z}), \text{ with } c_\mu(\mathbf{z}) = c(\chi_\mu(\mathbf{z})), \quad \chi_\mu(\mathbf{z}) = \text{LO}^\mu(D(\mathbf{z})), \quad (5)$$

where local optimization steps ($\mu > 0$) might be necessary for two reasons: Firstly, it is possible that the decoder D does not generate designs $D(\mathbf{z})$ for random latent space samples \mathbf{z} that fulfill all constraints of the optimization problem. The local optimization operator LO can then be used to enforce such constraints, an example of which is the mass constraint in the case of compliance minimization. And secondly, it is also possible that the decoded latent space X_Z does not contain the global optimum \mathbf{x}_{\min} but only goes through its basin X_{\min} . In such cases then, the best point $\chi_0(\mathbf{z}_0^*)$ included in X_Z might

be far away from the global optimum \mathbf{x}_{\min} (e.g., see **Fig. 4C**). By adding μ steps of local optimization, points closer to the global optimum can be explored during the optimization over the latent space, which increases the likelihood that the optimized point $\chi_{\mu}(z_{\mu}^*)$ reaches the global optimum at best or a point nearby at worst.

Adding local optimization also leads to certain issues, for instance making the cost function c_{μ} discontinuous and therefore limiting the optimization algorithms that can be used. But most importantly, the computational cost associated with this third step increases approximately linearly with value of μ . Depending on the time t_c necessary to evaluate this cost function c_{μ} , one could apply heuristic search methods like differential evolution (18) for inexpensive cost functions or Bayesian optimization (17) for more computationally involved ones.

Consequently, an optimal balance must then be struck between speed and proximity of $\chi_{\mu}(z_{\mu}^*)$ to the global optimum, for which μ has to be chosen carefully.

4. **Post-processing:** A local optimum $z^* = \operatorname{argmin} c_{\mu}(z)$ in latent space does not necessarily correspond to a local optimum in the design space (see Appendix 3.7 and **Fig. 4D**). Consequently, the solution $\chi_{\mu}(z_{\mu}^*)$ can likely be improved further by advancing it further towards the final solution \mathbf{x}^* by ν steps, resulting in

$$\mathbf{x}^* = \text{LO}^{\nu} \left(\chi_{\mu} \left(z_{\mu}^* \right) \right). \quad (6)$$

If different forms of local optimization are used for global optimization and post-processing, the following alternative is also possible, where the local optimization steps taken during the optimization over latent space are discarded:

$$\mathbf{x}^* = \text{LO}^{\nu} \left(D \left(z_{\mu}^* \right) \right). \quad (7)$$

Discussion

Optimization algorithms could exploit certain properties of the underlying cost function to increase their effectiveness. Some authors have recognized this while creating algorithms, for instance, for optimizing problems with non-deceptive gradients—*i.e.*, following the average

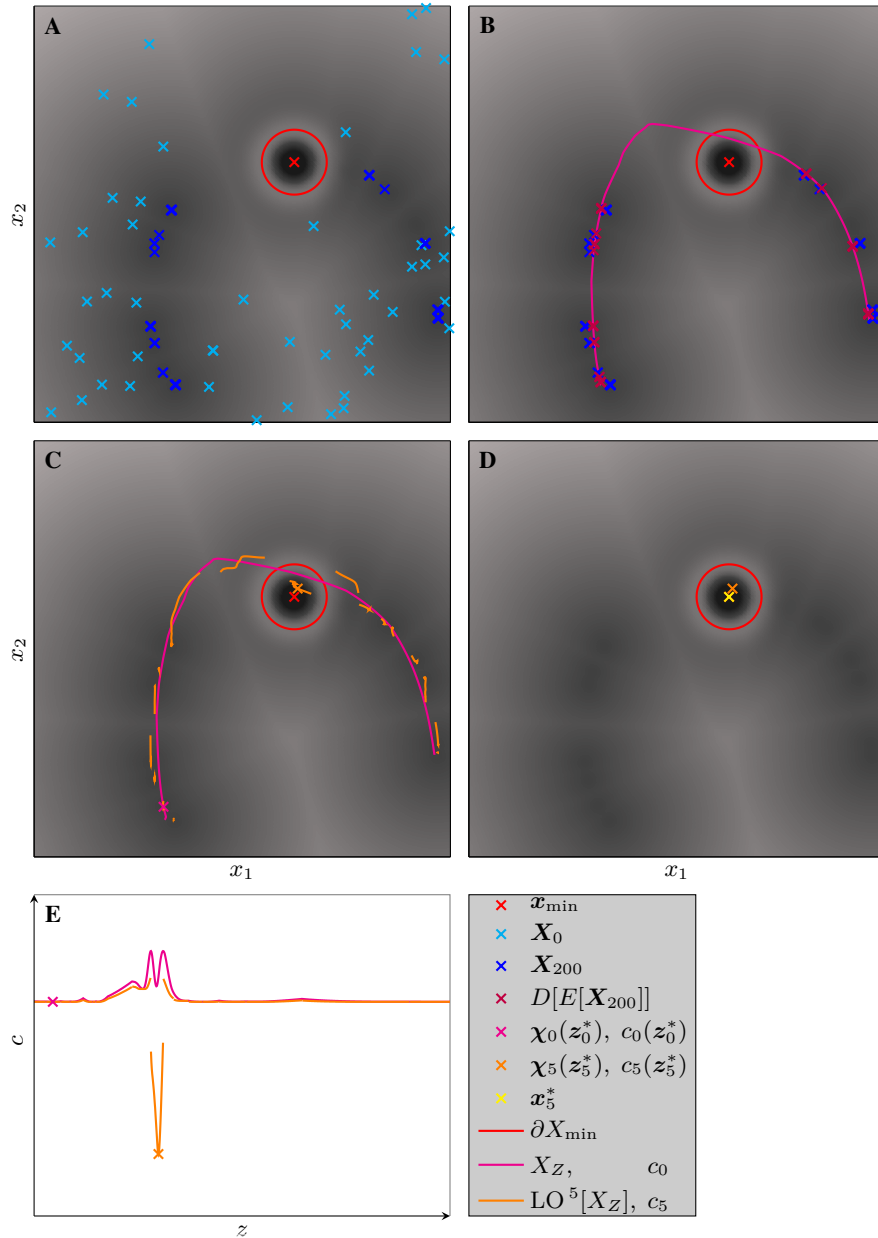


Fig. 4: A symbolic representation of the four steps of the proposed method for a case of $n = 2$ and $m = 1$. In the first step (A), a training set X_{200} is created by 200 iterations of gradient based local optimization, starting from random samples X_0 . An autoencoder is trained on this training set, leading to the decoded latent space X_Z (B). In the third step, global optimization over latent space can be performed (C+E). Here, the necessity for $\mu > 0$ is shown, as optimizing c_0 is not successful, while optimizing c_5 is. This can be seen in D, where the result of post-processing (x_5^*) is nearly identical to the global minimum x_{\min} .

slope of the cost function leads to the global optimum (62). Other authors simply ignore the cost function properties and simply tweak the optimization algorithm, for example by tuning hyperparameters to achieve a faster convergence on a limited set of benchmark problems (63, 64, 65, 8, 66). Nevertheless, because these benchmark problems are often constructed to be deceptive and/or random, the effectiveness of such procedures on real-world problems is at best questionable (62).

Contrary to other works in the literature involving autoencoders, our proposed method of autoencoder enabled global optimization procedure explicitly exploits the behavior of a certain class of cost functions. For these the global optimum can be found or at least better results are obtained when compared to other well-known optimization methods. For the compliance minimization problem in § **Compliance minimization**, for instance, the finite element discretization chosen has about 6.7×10^{1146} feasible sparse designs, and thus the design space is too vast to be fully explored using brute force methods. The proposed method, however, can exploit the structure of this problem because large regions of the search space are not interesting since topology optimization penalizes intermediate finite element densities (our design parameters), pushing them to either solid material or void. Furthermore, even sparse designs are unfeasible if their corresponding structure contains disconnected solid regions. As a result, it can be expected that the manifold that contains the global optimum and other feasible designs, has likely a far lower intrinsic dimensionality than that of the original design space, with an autoencoder hopefully being able to learn the features of the useful parts of the design space.

The use of the proposed method, however, comes at a high cost in time and computational resources, especially when compared to gradient-based approaches (which are the standard procedure for computationally-intensive problems such as structural optimization (67, 68, 69)). The potential of our method is thus most promising on problems where the cost function is highly non-convex, where gradient-based search would likely not lead to the optimum or any comparable design (70, 71, 72). Furthermore, the proposed method becomes attractive if a wealth of input data is already available, as this would drastically cut down on the time required for generating representative training samples for the autoencoder.

The proposed method is not without flaws, as it is difficult to determine if it can be applied at all. This results from the fact that there is no straightforward way to determine if a given cost

function fulfills the underlying assumptions of the method, *i.e.*, large parts of the search space are useless and can be discarded, with logical reasoning (as for example employed for § **Compliance minimization**) being our only option. And even if the assumption holds, determining the optimal hyperparameters for the method is difficult, especially in regard to the dimensionality of the latent space m . This is important, as decreasing m will in turn reduce the likelihood of finding the global optimum, while conversely, increasing m inevitably makes the optimization over latent space more time-consuming. While in this work m has been chosen by repeatedly running the procedure with increasing values of m , there is further room for improvement. For example, one could use inexpensive model order reduction methods—*e.g.*, principal component analysis (PCA)—to obtain an educated estimate for the number of features in the training data that the autoencoder has to reproduce (73). Further research could also be conducted to find possible trends for the optimal choice of other hyperparameters, like the required number of local optimization steps or the number of training samples. Other possible improvements are also imaginable. For example, it has been suggested that using the best designs generated with this proposed method as part of an updated sample set for a retraining of the autoencoder can lead to further improvements (48). Finally, the use of faster methods to generate appropriate training samples for the neural network in the first place would also increase the viability of this approach even further.

References

1. I. Newton, *Philosophiae naturalis principia mathematica*, vol. 2 (typis A. et JM Duncan, 1833).
2. J. Thøgersen, *European Psychologist* (2014).
3. J. G. Cho, J. S. Koo, H. S. Jung, *Journal of Mechanical Science and Technology* **30**, 673 (2016).
4. G. Zhao, Z. Liu, Y. He, H. Cao, Y. Guo, *Energy* **133**, 142 (2017).
5. D. M. Jiménez-Bravo, J. Pérez-Marcos, D. H De la Iglesia, G. Villarrubia González, J. F. De Paz, *Energies* **12** (2019).

6. F. Xiong, X. Zou, Z. Zhang, X. Shi, *Structural and Multidisciplinary Optimization* **62**, 3229 (2020).
7. J. Shalf, *Philosophical Transactions of the Royal Society A* **378** (2020).
8. W. Long, T. Wu, X. Liang, S. Xu, *Expert Systems with Applications* **123**, 108 (2019).
9. J. Pillardy, *et al.*, *Proceedings of the National Academy of Sciences* **98**, 2329 (2001).
10. J.-F. Chang, P. Shi, *Information Sciences* **181**, 2989 (2011).
11. S. Chen, J. Montgomery, A. Bolufé-Röhler, *Applied Intelligence* **42**, 514 (2015).
12. D. Guirguis, *et al.*, *IEEE Transactions on Evolutionary Computation* **24**, 613 (2020).
13. D. Molina, A. LaTorre, F. Herrera, *Cognitive Computation* **10**, 517 (2018).
14. M. S. Maučec, J. Brest, *Swarm and Evolutionary Computation* **50**, 100428 (2019).
15. D. H. Wolpert, W. G. Macready, *IEEE transactions on evolutionary computation* **1**, 67 (1997).
16. S. P. Adam, S.-A. N. Alexandropoulos, P. M. Pardalos, M. N. Vrahatis, *Approximation and optimization* pp. 57–82 (2019).
17. D. R. Jones, M. Schonlau, W. J. Welch, *Journal of Global optimization* **13**, 455 (1998).
18. R. Storn, K. Price, *Journal of global optimization* **11**, 341 (1997).
19. A. Zhigljavsky, A. Žilinskas, *Bayesian and High-Dimensional Global Optimization* (Springer Nature, 2021).
20. M. Amine Bouhleb, N. Bartoli, R. G. Regis, A. Otsmane, J. Morlier, *Engineering Optimization* **50**, 2038 (2018).
21. D. Eriksson, M. Pearce, J. Gardner, R. D. Turner, M. Poloczek, *Advances in Neural Information Processing Systems* **32**, 5496 (2019).
22. I. C. Cosme, I. F. Fernandes, J. L. de Carvalho, S. Xavier-de Souza, *Applied Mathematics and Computation* **328**, 125 (2018).

23. M. Mitchell, *An introduction to genetic algorithms* (MIT press, 1998).
24. J. Kennedy, R. Eberhart, *Proceedings of ICNN'95-International Conference on Neural Networks* (IEEE, 1995), vol. 4, pp. 1942–1948.
25. K. Kashima, *2016 IEEE 55th Conference on Decision and Control (CDC)* (2016), pp. 5750–5755.
26. D. Hartman, L. K. Mestha, *2017 IEEE Conference on Control Technology and Applications (CCTA)* (2017), pp. 1917–1922.
27. D. D'Agostino, A. Serani, E. F. Campana, M. Diez, *2018 AIAA/ASCE/AHS/ASC Structures, Structural Dynamics, and Materials Conference* (2018).
28. K. Lee, K. T. Carlberg, *Journal of Computational Physics* **404** (2020).
29. G. Kutyniok, P. Petersen, M. Raslan, R. Schneider, *Constructive Approximation* pp. 1–53 (2021).
30. R. Maulik, B. Lusch, P. Balaprakash, *Physics of Fluids* **33**, 037106 (2021).
31. G. E. Hinton, R. R. Salakhutdinov, *science* **313**, 504 (2006).
32. C. A. Floudas, C. E. Gounaris, *Journal of Global Optimization* **45**, 3 (2009).
33. P. Kora, P. Yadlapalli, *International Journal of Computer Applications* **162** (2017).
34. R. D. Al-Dabbagh, F. Neri, N. Idris, M. S. Baba, *Swarm and Evolutionary Computation* **43**, 284 (2018).
35. D. Wang, D. Tan, L. Liu, *Soft Computing* **22**, 387 (2018).
36. J. Snoek, H. Larochelle, R. P. Adams, *Advances in neural information processing systems* **25** (2012).
37. B. Shahriari, K. Swersky, Z. Wang, R. P. Adams, N. De Freitas, *Proceedings of the IEEE* **104**, 148 (2015).
38. L. F. C. A. Costa (2008).

39. V. Miranda, J. da Hora Martins, V. Palma, *IEEE Transactions on Power Systems* **29**, 3078 (2014).
40. Z. Gao, Z. Pan, J. Gao, Z. Xu, *SEG Technical Program Expanded Abstracts 2019* (Society of Exploration Geophysicists, 2019), pp. 1680–1684.
41. Z. Gao, *et al.*, *IEEE Transactions on Geoscience and Remote Sensing* pp. 1–15 (2020).
42. S. Eismann, S. Bartzsch, S. Ermon, Shape optimization in laminar flow with a label-guided variational autoencoder (2017).
43. Z. A. Kudyshev, A. V. Kildishev, V. M. Shalaev, A. Boltasseva, *Applied Physics Reviews* **7** (2020).
44. M. Tucci, S. Barmada, L. Sani, D. Thomopoulos, N. Fontana, *2019 International Applied Computational Electromagnetics Society Symposium (ACES)* (2019), pp. 1–2.
45. S. Barmada, N. Fontana, D. Thomopoulos, M. Tucci, *Applied Computational Electromagnetics Society Journal* **34** (2019).
46. Z. Yang, *et al.*, *Journal of Mechanical Design* **140** (2018).
47. C. C. Tutum, S. Chockchowwat, E. Vouga, R. Miikkulainen, *Proceedings of the Genetic and Evolutionary Computation Conference* (2018), pp. 1379–1386.
48. S. Oh, Y. Jung, S. Kim, I. Lee, N. Kang, *Journal of Mechanical Design* **141** (2019).
49. R.-R. Griffiths, J. M. Hernández-Lobato, *Chemical science* **11**, 577 (2020).
50. R. Martí, *Handbook of metaheuristics* (Springer, 2003), pp. 355–368.
51. L. Abualigah, A. Diabat, S. Mirjalili, M. Abd Elaziz, A. H. Gandomi, *Computer methods in applied mechanics and engineering* **376** (2021).
52. E. Andreassen, A. Clausen, M. Schevenels, B. S. Lazarov, O. Sigmund, *Structural and Multidisciplinary Optimization* **43**, 1 (2011).
53. D. P. Kingma, J. Ba, Adam: A method for stochastic optimization (2017).

54. O. Sigmund, *Structural and multidisciplinary optimization* **21**, 120 (2001).
55. J. A. Nelder, R. Mead, *The computer journal* **7**, 308 (1965).
56. I. P. Papadopoulos, P. E. Farrell, T. M. Surowiec, *SIAM Journal on Scientific Computing* **43**, A1555 (2021).
57. D. E. Rumelhart, G. E. Hinton, R. J. Williams., *Parallel Distributed Processing* **1** (1986).
58. M. A. Kramer, *AIChE journal* **37**, 233 (1991).
59. D. P. Kingma, M. Welling, Auto-encoding variational bayes (2014).
60. I. Goodfellow, *et al.*, *Advances in Neural Information Processing Systems* 27 (2014), pp. 2672–2680.
61. A. Makhzani, J. Shlens, N. Jaitly, I. Goodfellow, B. Frey, Adversarial autoencoders (2016).
62. W. Chu, X. Gao, S. Sorooshian, *Information Sciences* **181**, 4909 (2011).
63. S. Y. Yuen, C. K. Chow, *IEEE transactions on evolutionary computation* **13**, 454 (2008).
64. N. Noman, H. Iba, *IEEE Transactions on evolutionary Computation* **12**, 107 (2008).
65. W. Du, B. Li, *Information sciences* **178**, 3096 (2008).
66. Y. Sun, T. Yang, Z. Liu, *Applied Soft Computing* **85** (2019).
67. G. Marck, M. Nemer, J.-L. Harion, S. Russeil, D. Bougeard, *Numerical Heat Transfer, Part B: Fundamentals* **61**, 439 (2012).
68. W. Zuo, K. Saitou, *Structural and Multidisciplinary Optimization* **55**, 477 (2017).
69. H. Liu, D. Yang, P. Hao, X. Zhu, *Computer Methods in Applied Mechanics and Engineering* **342**, 625 (2018).
70. M. P. Bendsøe, O. Sigmund, *Topology optimization: theory, methods, and applications* (Springer Science & Business Media, 2003).
71. G. I. N. Rozvany, *Structural and Multidisciplinary Optimization* **37**, 217 (2009).

72. N. van Dijk, M. Langelaar, F. Van Keulen, *Proceedings of the 2nd International Conference on Engineering Optimization* (2010).
73. W. Chen, M. Fuge, J. Chazan, *Journal of Mechanical Design* **139** (2017).
74. M. P. Bendsøe, N. Kikuchi, *Computer Methods in Applied Mechanics and Engineering* **71**, 197 (1988).
75. M. P. Bendsøe, *Structural Optimization* **1**, 193 (1989).
76. E. J. Boers, H. Kuiper (1992).
77. K. O’Shea, R. Nash, *An introduction to convolutional neural networks* (2015).
78. D. Charte, F. Charte, S. García, M. J. del Jesus, F. Herrera, *Information Fusion* **44**, 78 (2018).
79. L. Wang, *et al.*, *Computer Methods in Applied Mechanics and Engineering* **372** (2020).
80. A. Makhzani, B. J. Frey, *Advances in Neural Information Processing Systems* 28 (2015), pp. 2791–2799.
81. A. Mondal, *et al.*, *Conference on Uncertainty in Artificial Intelligence* (PMLR, 2020), pp. 689–698.
82. X. Glorot, Y. Bengio, *Proceedings of the thirteenth international conference on artificial intelligence and statistics* (2010), pp. 249–256.
83. Y. Bengio, P. Lamblin, D. Popovici, H. Larochelle, *Advances in neural information processing systems* (2007), pp. 153–160.
84. Y. Zhou, D. Arpit, I. Nwogu, V. Govindaraju, *Is joint training better for deep auto-encoders?* (2015).
85. J. J. Park, P. Florence, J. Straub, R. Newcombe, S. Lovegrove, *IEEE Conference on Computer Vision and Pattern Recognition* (2019), pp. 165–174.
86. M. D. Hoffman, E. Brochu, N. de Freitas, *UAI* (Citeseer, 2011), pp. 327–336.

87. The authors would like to thank the Technical University Delft for supporting this work by making available its high-performance computing cluster for their use. Thanks also go to Professor Fred van Keulen for suggesting the use of signed distance field as a method of encoding.

Supplementary materials

The supplementary materials include

1	Computational methods	23
1.1	SIMP	23
1.2	Feed-forward neural networks	26
1.3	Autoencoder	29
1.4	Pretraining	32
1.5	Signed distance field	33
2	Implementation of numerical simulations	34
2.1	Minimizing c_1 from § Benchmark functions	34
2.2	Minimizing c_2 , c_3 , and c_4 from § Benchmark functions	38
2.3	Compliance minimization	39
2.4	Design variations for compliance minimization	43
3	Supplementary text	44
3.1	Intrinsic dimensionality of an optimization problem	44
3.2	On the average number of tries until success	46
3.3	Intrinsic dimensionality of c_1 from § Benchmark functions	46
3.4	Results for c_3 and c_4 from § Benchmark functions	47
3.5	On the size of the design space in § Compliance minimization	48
3.6	Evaluation time for the optimization over latent space for § Compliance minimization	48
3.7	On the need for post-processing	49

1 Computational methods

1.1 SIMP

The solid isoparametric material with penalization (SIMP) is a method used for gradient-based topology optimization, first proposed by Bendsøe in the late 1980s (74, 75). In this work, it is

used to solve the compliance minimization problem:

$$\begin{aligned} \mathbf{x}_{\min} &= \underset{\mathbf{x}_i \in X = [0,1]^{n_y \times n_x}}{\operatorname{argmin}} \quad C(\mathbf{x}_i) = \mathbf{U}^\top \mathbf{K} \mathbf{U}, \\ \text{subject to: } & \mathbf{K} \mathbf{U} = \mathbf{F}, \\ & \rho(\mathbf{x}_i) \leq \rho_0, \end{aligned} \quad (8)$$

where \mathbf{K} is the stiffness matrix and \mathbf{F} the force vector, \mathbf{U} is the displacement degree of freedom vector, $\rho_0 = 0.4$ is the maximum density, and $\rho(\mathbf{x}_i)$ the density if the i th design calculated as

$$\rho(\mathbf{x}_i) = \frac{1}{n_y n_x} \sum_{j=1}^{n_y \times n_x} x_j, \quad (9)$$

and x_j denotes the j th component of vector \mathbf{x}_i . SIMP is then used to advance from an initial material distribution \mathbf{x}_0 to a final distribution \mathbf{x}_λ . To advance the design from from $\mathbf{x}_i^{(k)}$ to $\mathbf{x}_i^{(k+1)}$, the following iterative step has to be taken:

- The stiffness matrix $\mathbf{K}_i = \mathbf{K}(\mathbf{x}_i)$ has to be constructed (for an fast assembly see Andreassen *et al.* (52)). For each element we use a Poisson's ration $\nu_j = \nu_0 = 0.3$ and a Young's modulus of E_j , with a penalization parameter $p = 3$ and $E_0 = 1$

$$E_j = E_0 \left(\frac{1}{10\,000} + \frac{9999}{10\,000} x_j^p \right). \quad (10)$$

This transformation ensures that $E_j = 0$ is not possible and that the stiffness matrix will not be singular. We then find the displacement vector \mathbf{U}_i by solving the system $\mathbf{K}_i \mathbf{U}_i = \mathbf{F}$, from which the compliance is computed as $C_i = \mathbf{U}_i^\top \mathbf{F}$.

- The sensitivity S_i of the i th design is calculated component-wise as

$$\begin{aligned} S_j &= -\frac{\partial C_i}{\partial x_j} \\ &= -\frac{9999}{10\,000} E_0 p x_j^{p-1} \mathbf{U}_i^\top \frac{\partial \mathbf{K}_i}{\partial E_j} \mathbf{U}_i. \end{aligned} \quad (11)$$

For details on the assembly of \mathbf{K}_i and the derivative $\partial \mathbf{K}_i / \partial E_j$ see Andreassen *et al.* (52).

- If only the sensitivity is used to update the design, then SIMP often leads to a checkerboard pattern. As such a design is not manufacturable, one of the following methods can be used to update the sensitivity to \mathbf{G}_i :

- A filter on the design can be used, which is characterized by the filter radius $r_{\min} > 1$ (see Andreassen *et al.* (52)).

- By setting $r_{\min} \in (0, 1]$, the filter will have no effect. In this case, the sensitivity of the Ginzburg-Landau energy term could be added to S_i to avoid the checkerboarding (see Papadopoulos *et al.* (56)):

$$G_j = S_j x_j + \frac{\beta}{\epsilon} (1 - 2x_{k,l}) + \beta \epsilon (4x_{k,l} - x_{k-1,l} - x_{k+1,l} - x_{k,l-1} - x_{k,l+1}), \quad (12)$$

where subscripts indicate the values of neighboring elements in the 2D mesh, *e.g.*, $x_{k,l-1}$ is the value of the element immediately to the left of the element $x_{k,l} \equiv x_j$, while the parameters $\beta = 0.05$ and ϵ are used to tune the process.

When using SIMP in this work, the latter approach is used.

- To avoid generating repeated training samples, a method called deflation is used for every instance of SIMP in this work (56). In this approach, G_i is updated with

$$G_i = G_i - 50 \sum_{h=1}^{\delta} \frac{\mathbf{x}_i - \mathbf{x}_{D,h}}{\langle (\mathbf{x}_i - \mathbf{x}_{D,h}), (\mathbf{x}_i - \mathbf{x}_{D,h}) \rangle_F^2}, \quad (13)$$

which pushes new samples away from already explored designs $\mathbf{X}_{D,\delta} = \{\mathbf{x}_{D,1}, \dots, \mathbf{x}_{D,\delta}\}$

- Lastly we improve the design by computing D_i , with components

$$D_j = \sqrt{G_j x_j}. \quad (14)$$

An iterative process is started, with $l_l^{(0)} = 0$ and $l_u^{(1)} = 1\,000\,000$. The components of the design $\mathbf{x}_i^{(k+i)}$ for the next iteration are computed as

$$x_j^{(k+i)} = \max \left\{ \min \left\{ \frac{2D_j}{l_l^{(k)} + l_u^{(k)}}, x_j^{(k)} + 0.25, 1 \right\}, x_j^{(k)} - 0.25, 0.0001 \right\},$$

$$\{l_l^{(k+1)}, l_u^{(k+1)}\} = \begin{cases} \left\{ l_l^{(k)}, \frac{l_l^{(k)} + l_u^{(k)}}{2} \right\} & \rho(\mathbf{x}_i) \leq \rho_0, \\ \left\{ \frac{l_l^{(k)} + l_u^{(k)}}{2}, l_u^{(k)} \right\} & \rho(\mathbf{x}_i) > \rho_0. \end{cases} \quad (15)$$

This will be done while the following condition is fulfilled, after which one has the next step $\mathbf{x}_i^{(k+1)}$:

$$\frac{l_{u,j} - l_{l,j}}{l_{u,j} + l_{l,j}} > 0.0001. \quad (16)$$

Due to the penalization $p > 1$, using intermediate values for the density is disadvantageous, and the final outcome will likely be sparse. When employing a step of SIMP, the notation

$\text{SIMP}_{\epsilon, \mathbf{X}_{D, \delta}}$ is used, where ϵ is the parameter for the Ginzburg-Landau energy sensitivity (see equation (12)) and $\mathbf{X}_{D, \delta}$ is the set of previous solutions that are to be avoided (see equation (13)).

1.2 Feed-forward neural networks

An artificial neural network is in its most basic form simply a graph of connected nodes, which in some capacity tries to model the behavior of human brains (76). In the case of a feed-forward neural network, these nodes, which are also known as neurons, each belong to different layers $\mathbf{y}^{(l)}$ with $l \in \{0, \dots, L\}$. $\mathbf{y}^{(0)}$ is commonly called the input layer, while $\mathbf{y}^{(L)}$ is referred to as output layer. Layers in between are known as hidden layers. These layers are connected by often nonlinear functions $f_{\theta^{(l)}}^{(l)}$, which are dependent on a number of parameters $\theta^{(l)}$. To wit,

$$\mathbf{y}^{(l)} = f_{\theta^{(l)}}^{(l)}(\mathbf{y}^{(l-1)}). \quad (17)$$

Consequently, a feed-forward neural network can also be seen as a number of function compositions:

$$\mathbf{x}^{(L)} = (f_{\theta^{(L)}}^{(L)} \circ \dots \circ f_{\theta^{(1)}}^{(1)})(\mathbf{y}^{(0)}) \quad (18)$$

Many different functions have been proposed (77), with most of them relying on the so called activation function $\sigma^{(l)}$, of which the following four types are used in this work:

$$\begin{aligned} \sigma_I(x) &= x, \\ \sigma_S(x) &= \frac{1}{1 + \exp(-x)}, \\ \sigma_T(x) &= \tanh(x), \\ \sigma_R(x) &= \begin{cases} x & x \geq 0, \\ 0.3x & x < 0 \end{cases} \end{aligned} \quad (19)$$

In this work, six types of connections $f_{\theta^{(l)}}^{(l)}$ are used:

- **Dense connection** One possibility to connect two layers is the dense connection (\mathbb{O}_{Δ}). In this case, each element (also called neuron) $y_i^{(l-1)}$ with $i \in \{1, \dots, \nu^{(l-1)}\}$ of layer $\mathbf{y}^{(l-1)} \in \mathbb{R}^{\nu^{(l-1)}}$ is connected to every neuron $y_j^{(l)}$ of the layer $\mathbf{y}^{(l)}$ by the weight $w_{ji}^{(l)}$ ($\mathbf{W}^{(l)} \in \mathbb{R}^{\nu^{(l)} \times \nu^{(l-1)}}$). Additionally, each neuron $y_j^{(l)}$ has a bias value $b_j^{(l)}$ ($\mathbf{b}^{(l)} \in \mathbb{R}^{\nu^{(l)}}$), and the activation function $\sigma^{(l)}$ is used as well:

$$\mathbf{y}^{(l)} = f_{\theta^{(l)}}^{(l)}(\mathbf{y}^{(l-1)}) = \sigma^{(l)}[\mathbf{W}^{(l)}\mathbf{x}^{(l-1)} + \mathbf{b}^{(l)}]. \quad (20)$$

This function is therefore parameterized by $\theta^{(l)} = \{\mathbf{W}^{(l)}, \mathbf{b}^{(l)}\}$.

- **Convolutional connection:** A different type of connection between two layers is the convolutional one (\mathbb{O}_C). Instead of the dense layer, which is mainly used to connect two one-dimensional vectors, a convolutional function in this work connects two layers consisting of three-dimensional tensors. Each neuron $y_{ijk}^{(l)}$ is part of row $i \in \{1, \dots, \nu_y^{(l)}\}$, column $j \in \{1, \dots, \nu_x^{(l)}\}$, as well as channel $k \in \{1, \dots, \kappa^{(l)}\}$, with $\mathbf{y}^{(l)} \in \mathbb{R}^{\nu_y^{(l)} \times \nu_x^{(l)} \times \kappa^{(l)}}$.

In a convolutional connection, each channel k of the layer $\mathbf{y}^{(l-1)}$ is connected to every channel c of the layer $\mathbf{y}^{(l)}$ by a filter $\mathbf{K}_{ck}^{(l)} \in \mathbb{R}^{t_y^{(l)} \times t_x^{(l)}}$. Here, $t_y^{(l)} \times t_x^{(l)}$ is the filter size. While rectangular filters are possible, it is common to use quadratic filters ($t_y^{(l)} = t_x^{(l)} = t^{(l)}$), which is done mostly in this work as well.

For every node $y_{ijc}^{(l)}$, a part of $\mathbf{x}_k^{(l-1)}$, namely $\vartheta_{ijk}^{(l-1)}$ (chosen depending on filter size $t^{(l)}$ and stride $s^{(l)}$, see **Fig. 5**), has this filter applied. The results of this for all k are added, and a bias $b_{ijc}^{(l)}$ is applied as well as an activation function:

$$y_{ijc}^{(l)} = \sigma^{(l)} \left(b_c^{(l)} + \sum_{k=1}^{\kappa^{(l-1)}} \langle \vartheta_{ijk}^{(l-1)}, \mathbf{K}_{ck}^{(l)} \rangle_F \right), \quad (21)$$

where $\langle \cdot, \cdot \rangle_F$ denotes the Frobenius inner product. Consequently, the parameters $\theta^{(l)} = \{\mathbf{K}^{(l)}, \mathbf{b}^{(l)}\}$ define the function $f_{\theta^{(l)}}^{(l)}$, with $\mathbf{K}^{(l)} \in \mathbb{R}^{\kappa^{(l)} \times \kappa^{(l-1)} \times t_y^{(l)} \times t_x^{(l)}}$.

- **Max-pooling connection:** Similar to the convolutional connection is the max pooling connection (\mathbb{O}_M). Depending on filter sizes $t_y^{(l)}$ and $t_x^{(l)}$ and stride $s^{(l)}$, a pooled area $\vartheta_{ijk}^{(l-1)}$ is chosen. One can then determine:

$$y_{ijc}^{(l)} = \max \left(\vartheta_{ijk}^{(l-1)} \right). \quad (22)$$

In this case, the function $f_{\theta^{(l)}}^{(l)}$ has an empty parameter set $\theta^{(l)} = \emptyset$. The activation function used here is normally the identity one σ_I , so it has not been depicted in equation (22).

- **Deconvolutional connection:** Also used in this work is the deconvolutional connection (\mathbb{O}_D). Here, similarly to $\vartheta_{ijk}^{(l-1)}$ and $y_{ijc}^{(l)}$ in the previous cases, $\vartheta_{ijc}^{(l)}$ can be determined for a node $y_{ijk}^{(l-1)}$, based on filter sizes $t_y^{(l)}$ and $t_x^{(l)}$ and stride $s^{(l)}$:

$$\vartheta_{ijc}^{(l)} = \sum_{k=1}^{\kappa^{(l-1)}} \mathbf{K}_{ck}^{(l)} y_{ijk}^{(l-1)}. \quad (23)$$

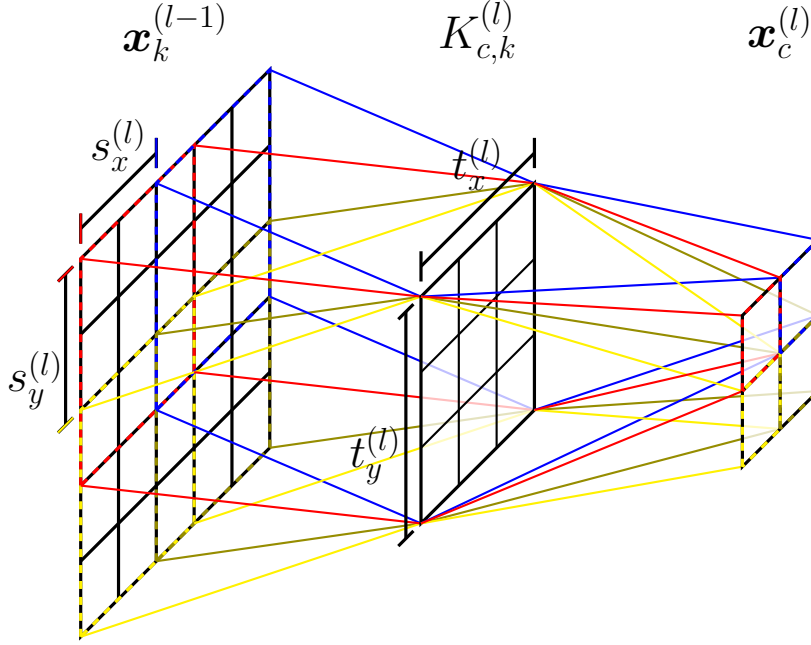


Fig. 5: Representation of a convolutional connection between the channels $\mathbf{x}_k^{(l-1)}$ and $\mathbf{x}_c^{(l)}$, using the filter $K_{c,k}^{(l)}$, and a stride $s_y^{(l)} = s_x^{(l)} = 2$, as well as a filter size $t_y^{(l)} = t_x^{(l)} = 3$. In this work, $t_y^{(l)} = t_x^{(l)} = t^{(l)}$ will always be the case.

Here, $\mathbf{v}_{1,1,k}^{(l-1)}$ and $x_{1,1,c}^{(l)}$ are seen in red boundaries in $\mathbf{x}_k^{(l-1)}$ and $\mathbf{x}_c^{(l)}$ respectively. Similarly, $\mathbf{v}_{2,1,k}^{(l-1)}$ and $x_{2,1,c}^{(l)}$ are surrounded in yellow, $\mathbf{v}_{1,2,k}^{(l-1)}$ and $x_{1,2,c}^{(l)}$ in blue, and $\mathbf{v}_{2,2,k}^{(l-1)}$ and $x_{2,2,c}^{(l)}$ in green.

Finally, the channel $\mathbf{y}_c^{(l)}$ has to be assembled (using the assembly operator \mathbb{A} , which adds values from the local matrix $\mathbf{v}_{ijc}^{(l)}$ to the global one $\mathbf{y}_c^{(l)}$), with $i \in \{1, \dots, \nu_y^{(l-1)}\}$ and $j \in \{1, \dots, \nu_x^{(l-1)}\}$:

$$\mathbf{y}_c^{(l)} = \sigma^{(l)} \left[\mathbf{1}b_c^{(l)} + \mathbb{A}_{i,j} \mathbf{v}_{ijc}^{(l)} \right]. \quad (24)$$

Here, $\mathbf{1}$ is a matrix of the size of $\mathbf{y}_c^{(l)}$ with the value of 1 at every element. This function is consequently parameterized by $\boldsymbol{\theta}^{(l)} = \{\mathbf{K}^{(l)}, \mathbf{b}^{(l)}\}$.

A problem for deconvolutional connections is padding, as it is possible that there are elements in $\mathbf{y}_c^{(l)}$ for which there are no corresponding $\mathbf{v}_{ijc}^{(l)}$, setting them automatically to assume the value $b_c^{(l)}$. This can be avoided by using, as was done in this work, $\nu_x^{(l-1)} = s_x^{(l)}(\nu_x^{(l)} - 1) + t_x^{(l)}$ and $\nu_y^{(l-1)} = s_y^{(l)}(\nu_y^{(l)} - 1) + t_y^{(l)}$ for convolutional or max pooling connections, as well as $\nu_x^{(l)} = s_x^{(l)}(\nu_x^{(l-1)} - 1) + t_x^{(l)}$ and $\nu_y^{(l)} = s_y^{(l)}(\nu_y^{(l-1)} - 1) + t_y^{(l)}$ for deconvolutional connections.

- **Flattening connection:** A connection \mathbb{O}_F , used to flatten a layer from a three-dimensional

tensor to a one-dimensional representation ($\nu_y^{(l-1)}\nu_x^{(l-1)}\kappa^{(l-1)} = \nu^{(l)}$), is also needed:

$$\mathbb{O}_F = f^{(l)} : \mathbb{R}^{\nu_y^{(l-1)} \times \nu_x^{(l-1)} \times \kappa^{(l-1)}} \rightarrow \mathbb{R}^{\nu_y^{(l-1)}\nu_x^{(l-1)}\kappa^{(l-1)}}. \quad (25)$$

- **Inverse flattening connection:** Lastly, the ability to transform a one-dimensional layer back into a three-dimensional one is also needed, for which we use \mathbb{O}_I and which can be considered as an inversion of \mathbb{O}_F , with $\nu_y^{(l)}\nu_x^{(l)}\kappa^{(l)} = \nu^{(l-1)}$ being a condition to be fulfilled:

$$\mathbb{O}_I(\nu_y^{(l)}, \nu_x^{(l)}, \kappa^{(l)}) = f^{(l)} : \mathbb{R}^{\nu^{(l-1)}} \rightarrow \mathbb{R}^{\nu_y^{(l)} \times \nu_x^{(l)} \times \kappa^{(l)}}, \quad (26)$$

$$\left(\mathbb{O}_I(\nu_y^{(l)}, \nu_x^{(l)}, \kappa^{(l)}) \circ \mathbb{O}_F\right) \left(\mathbf{y}^{(l)}\right) = \mathbf{y}^{(l)}. \quad (27)$$

1.3 Autoencoder

An autoencoder is a special type of feed-forward neural network (see Appendix 1.2), first proposed by Rumelhart *et al.* (57) and improved by Kramer (58). An autoencoder, in its most basic form, is distinguished by two characteristic properties:

- Firstly, the input layer $\mathbf{y}^{(0)}$ and the output layer $\mathbf{y}^{(L)}$ have the same dimensionality. In this work, the input layer will be denoted as $\mathbf{x} = \mathbf{y}^{(0)}$, while the output layer will be $\mathbf{x}_{\text{AE}} = \mathbf{y}^{(L)}$. The goal of the autoencoder is to be trained in such a way to minimize the difference between input and output for some training data.
- An autoencoder has at least one hidden layer ($L > 1$) with fewer nodes than those of input and output layers. The hidden layer l_B with the lowest number of nodes, which is commonly known as the bottleneck layer, is usually named $\mathbf{z} = \mathbf{y}^{(l_B)} \in \mathbb{R}^m$.

It is possible to split the autoencoder network into two separate networks, the encoder E and the decoder D (see **Fig. 6A**):

$$\begin{aligned} E_{\theta_E} &= \left(f_{\theta^{(l_B)}}^{(l_B)} \circ \dots \circ f_{\theta^{(1)}}^{(1)}\right), & \theta_E &= \left\{\theta^{(1)}, \dots, \theta^{(l_B)}\right\}, \\ D_{\theta_D} &= \left(f_{\theta^{(L)}}^{(L)} \circ \dots \circ f_{\theta^{(l_B+1)}}^{(l_B+1)}\right), & \theta_D &= \left\{\theta^{(l_B+1)}, \dots, \theta^{(L)}\right\}. \end{aligned} \quad (28)$$

In this work, the domain of input and output layers is referred to as the design space X ($\mathbf{x}, \mathbf{x}_{\text{AE}} \in X$), while the domain of \mathbf{z} is the latent space Z ($\mathbf{z} \in Z$). The following can then be assumed:

$$\mathbf{x}_{\text{AE}} = D_{\theta_D}(\mathbf{z}) = D_{\theta_D}(E_{\theta_E}(\mathbf{x})) \quad (29)$$

The corresponding reconstruction loss function $\mathcal{L}_{R,i}$ for a single sample \mathbf{x}_i is then the mean squared error, where \mathbf{W}_i is the corresponding weight matrix:

$$\mathcal{L}_{R,i}^{E,D} = \langle \mathbf{W}_i, (\mathbf{x}_i - D(E(\mathbf{x}_i)))^2 \rangle_F. \quad (30)$$

The E, D in the superscript of the loss function indicate which network parameters are optimized depending on this loss, which in this case are the encoder E and decoder D networks. Depending on the number of hidden layers, autoencoders can be discriminated into deep ($L > 2$) and shallow ($L = 2$) autoencoders (78). Although using only encoder E and decoder D networks is possible, expanding the network might be advantageous, with different possibilities and their benefits being explored in the following paragraphs (42, 79, 43). Four different network architectures have been proposed (see **Fig. 6**):

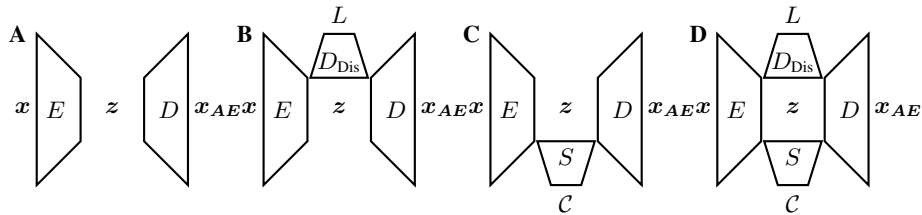


Fig. 6: A depiction of different autoencoder networks with encoder E and decoder D . In **A**, a simple autoencoder is seen. In **B**, through the addition of a discriminator network D_{Dis} an adversarial autoencoder is seen. On the other hand, in **C**, one added a surrogate network S instead. In **D**, the final possible combination is depicted, an adversarial autoencoder with surrogate network.

- When using an additional discriminator network D_{Dis} , the expanded architecture is known as an adversarial autoencoder (80). The main purpose of its use is to enforce a certain distribution of the encoded training samples in latent space, which would lead to feasible designs being produced over the whole latent space (43). Additionally, using a discriminator might also lead to a more even distribution of local minima and maxima of the function $c_\mu(\mathbf{z})$ (see Equation (5)), which would be advantageous for a successful optimization over latent space. While adversarial autoencoders are similar in that purpose to generative adversarial networks (60), they do not suffer from mode collapse (81), meaning that they do not randomly loose features of the training data, and allow for easier training due to the lower-dimensional input of the discriminator network (43). To achieve this, the discriminator maps a latent space representation \mathbf{z} onto the likelihood $L = D_{Dis}(\mathbf{z}) \in [0, 1]$ that

it has been generated according to the desired probability distribution \mathcal{Z}_D , which might be normal or uniform distribution (although more complex ones, especially for labeled data, can be used (80)). To achieve this, the discriminator is trained to differentiate between two different sources for latent space samples, namely random samples ($\mathbf{z}_i \sim \mathcal{Z}_D$) and encoded training set samples ($E(\mathbf{x}_i)$ with $\mathbf{x}_i \in \mathbf{X}_\lambda$). The training optimizes the parameters $\theta_{D_{\text{Dis}}}$ of the discriminator by means of the following loss function:

$$\mathcal{L}_{D1,i}^{D_{\text{Dis}}} = \frac{1}{2} (\ln (D_{\text{Dis}}(E(\mathbf{x}_i))) + \ln (1 - D_{\text{Dis}}(\mathbf{z}_i))), \quad (31)$$

This forces the discriminator to put out $D_{\text{Dis}}(E(\mathbf{x}_i)) \rightarrow 0^+$ for samples originating from the training set, while samples generated according to the desired distribution are forced towards $D_{\text{Dis}}(\mathbf{z}_i) \rightarrow 1^-$.

The encoder meanwhile is trained to fool the discriminator by minimizing the loss function

$$\mathcal{L}_{D2,i}^E = \ln (1 - D_{\text{Dis}}(E(\mathbf{x}_i))), \quad (32)$$

so that $D_{\text{Dis}}(E(\mathbf{x}_i))$ tends towards $L = 1$. These two loss functions are then each added to the overall loss function of the network for each batch with a probability of P_{Dis} , so that none, one or both of the loss functions can be used to update the network parameters in each batch. The corresponding network architectures that use D_{Dis} are shown schematically in **Figs. 6B** and **Figs. 6D**.

- One can also add a surrogate network S , which maps a latent space vector \mathbf{z} onto the cost function approximation $\mathcal{C} = S(\mathbf{z}) \in [0, 1]$. This could enforce a improved separation between better and worse samples in latent space, possibly reducing the number of local minima for $c(D(\mathbf{z}))$, which would allow for a faster optimization (42, 79). The surrogate network is then trained to reproduce the scaled cost function value $c(\mathbf{x})$:

$$\begin{aligned} c_{n,i} &= \frac{1}{10} + \frac{8}{10} \frac{c(\mathbf{x}_i) - c_{\min}}{c_{\max} - c_{\min}}, \\ c_{\min} &= \min_{\mathbf{x}_i \in \mathbf{X}_\lambda} c(\mathbf{x}_i), \\ c_{\max} &= \max_{\mathbf{x}_i \in \mathbf{X}_\lambda} c(\mathbf{x}_i). \end{aligned} \quad (33)$$

The following loss function is then used to train the encoder E and the surrogate model

S to that end:

$$\mathcal{L}_{\text{sur},i}^{E,S} = \beta_S (c_{n,i} - S(E(\mathbf{x}_i)))^2. \quad (34)$$

This loss function is added to the overall loss function of the whole network. Network architectures that use S are shown schematically in **Fig. 6C** and **Fig. 6D**.

To train the neural networks in this work, backpropagation and gradient based optimization is used. This makes the performance of the trained networks dependent on the initial parameters set in the networks. Bias vectors were initialized as zero, while weight tensors $\mathbf{W}^{(l)}$ and filters $\mathbf{K}^{(l)}$ are set using Xavier initialization (82). After initializing the network parameters θ_0 , batch gradient descent is used to optimize the network parameters over multiple epochs. Adam (53) is used to update the network parameters after every batch from, using a learning rate of $\alpha = 0.001$, as well as decay rates $\beta_1 = 0.9$ and $\beta_2 = 0.999$.

1.4 Pretraining

For autoencoder networks, there is always the possibility of using pretraining for the encoder E and decoder D . This has been shown to improve the autoencoder performance, although there is conflicting evidence (83, 84).

For pretraining to be possible, the encoder E and decoder D need layers with the same dimensionality. This would then allow one to split up both into n_{pre} smaller networks E_i and D_i , where the input layer of E_i and the output layer of D_i would have the same dimension, as well as the output layer of E_i and the input layer of D_i :

$$\begin{aligned} E &= (E_{n_{\text{pre}}} \circ \dots \circ E_1) \\ D &= (D_1 \circ \dots \circ D_{n_{\text{pre}}}) \end{aligned} \quad (35)$$

One could then train these smaller networks, beginning with E_1 and D_1 and then going inwards from there, by minimizing either the loss function

$$\mathcal{L}_{\text{pre1},i}^{E_j,D_j} = \rho \left((\mathbf{x}_i - (D_1 \circ \dots \circ D_j \circ E_j \circ \dots \circ E_1)(\mathbf{x}_i))^2 \right) \quad (36)$$

or

$$\mathcal{L}_{\text{pre2},i}^{E_j,D_j} = \rho \left(((E_{j-1} \circ \dots \circ E_1)(\mathbf{x}_i) - (D_j \circ E_j \circ \dots \circ E_1)(\mathbf{x}_i))^2 \right). \quad (37)$$

While the first loss function overall leads to smaller losses, this is achieved by a longer calculation time. Therefore, in this work, $\mathcal{L}_{\text{pre2}}$ is used for pretraining.

1.5 Signed distance field

The main goal of the autoencoder is to reproduce the input layer at the output layer as closely as possible. In the case of topology optimization problems (see § **Compliance minimization** for an example), the boundaries of the design between material and void are most important. To allow the autoencoder to mainly focus on these parts of the design, a transformation $\text{SDF}(\boldsymbol{x}) : [0, 1]^{n_y \times n_x} \rightarrow \mathbb{R}^{n_y \times n_x}$ to a quasi-signed distance field is created, which might lead to a better autoencoder performance (85). The SDF function itself consists out of two steps:

- In the first step a design \boldsymbol{x} is transformed into $\boldsymbol{\psi}$, with components

$$\psi_j = \begin{cases} -A & x_j \leq 0.002, \\ x_j - 0.5 & 0.002 < x_j \leq 0.998, \\ A & 0.998 < x_j, \end{cases} \quad (38)$$

where $A = 2\sqrt{n_y^2 + n_x^2}$ is used. Such values indicate elements for which a distance value cannot yet be determined, with this specific value for A being used as it cannot occur naturally as a distance measurement in a mesh of the size $n_y \times n_x$.

- In a second step we iterate over the mesh elements whose absolute value $|\psi_j| = A$. These components are updated by firstly constructing the matrix

$$\boldsymbol{\Psi}_j = \text{sgn}(\psi_{k,l}) \begin{pmatrix} \psi_{k-1,l-1} & \psi_{k-1,l} & \psi_{k-1,l+1} \\ \psi_{k,l-1} & \psi_{k,l} & \psi_{k,l+1} \\ \psi_{k+1,l-1} & \psi_{k+1,l} & \psi_{k+1,l+1} \end{pmatrix}, \quad (39)$$

where subscripts indicate the values of neighboring elements in the 2D mesh, *e.g.*, $\psi_{k-1,l-1}$ is the value of the element immediately to the upper left of the element $\psi_{k,l} \equiv \psi_j$. If a component of $\boldsymbol{\Psi}$ does not exist in $\boldsymbol{\psi}$, the closest value is taken instead. For example, $\psi_{0,1}$, which does not exist in the mesh, is replaced by $\psi_{1,1}$, which does. Meanwhile, we define a filter matrix \mathcal{F} as

$$\mathcal{F} = \begin{pmatrix} \sqrt{2} & 1 & \sqrt{2} \\ 1 & 0 & 1 \\ \sqrt{2} & 1 & \sqrt{2} \end{pmatrix}. \quad (40)$$

The components of matrix $\boldsymbol{\Psi}_j$, denoted as $[\Psi_j]_{ab}$, are then updated as

$$[\Psi_j]_{ab} = \max \left\{ [\Psi_j]_{ab}, -\frac{1}{2} \mathcal{F}_{ab} \right\}. \quad (41)$$

This allows the calculation of the final result

$$\psi_j \equiv \text{sgn}(\psi_j) \min_{a,b} \left([\Psi_j]_{ab} + \mathcal{F}_{ab} \right). \quad (42)$$

This step, done for every value of ψ is then repeated until $\max(|\psi_j|) < A$. The final outcome $\psi = \text{SDF}(\mathbf{x})$ is so obtained.

To transform signed distance fields back into density fields, we use the function $\text{SDF}^{-1} : \mathbb{R}^{n_y \times n_x} \rightarrow [0, 1]^{n_y \times n_x}$ with $\text{SDF}^{-1}(\text{SDF}(\mathbf{x})) = \mathbf{x}$:

$$\text{SDF}^{-1}(\psi_j) = \begin{cases} 0 & \psi_j \leq -0.5, \\ \psi_j + 0.5 & -0.5 < \psi_j \leq 0.5, \\ 1 & 0.5 < \psi_j. \end{cases} \quad (43)$$

It has to be noted that, if the signed distance field is used, \mathbf{x}_i has to be replaced with $\text{SDF}(\mathbf{x}_i)$ in the loss functions (30), (31), (32), (34), (36), and (37).

2 Implementation of numerical simulations

2.1 Minimizing c_1 from § Benchmark functions

A function c_1 is designed in multiple steps to test the viability of the proposed method.

1. In an 10 dimensional space ($\mathcal{Z} = [0, 1]^{10}$), 2500 random points $\zeta_i \in \mathcal{Z}$ are generated. These points $\zeta = \{\zeta_1, \dots, \zeta_{2500}\}$ are then saved.
2. A mapping $T_D : \mathbb{R}^M \rightarrow \mathbb{R}^n$ is created, which allows to find $\mathbf{x}_i \in \mathbb{R}^n$ from ζ_i with

$n = 1000$:

$$\begin{aligned}
\mathbf{x}_{1,i} &= \tanh [\mathbf{W}_1 \boldsymbol{\zeta}_i + \mathbf{b}_1], \\
\mathbf{x}_{2,i} &= \exp [- (\mathbf{W}_2 \mathbf{x}_{1,i} + \mathbf{b}_2) \odot (\mathbf{W}_2 \mathbf{x}_{1,i} + \mathbf{b}_2)], \\
[x_{3,i}]_j &= \frac{2}{1 - [b_3]_j} ([x_{2,i}]_j - [b_3]_j) - 1, \\
\mathbf{x}_{4,i} &= \mathbf{W}_4 \mathbf{x}_{3,i} + \mathbf{b}_4, \\
\mathbf{x}_{5,i} &= \frac{4}{5} \tanh [\mathbf{x}_{4,i} - \mathbf{x}_{4,1}], \\
[x_i]_j &= \left(\frac{3}{4} [x_{5,i}]_j - \frac{1}{4} \right) ([x_{5,i}]_j^2 - 1) + \frac{2}{\pi} \arcsin ([x_{5,i}]_j), \\
\mathbf{W}_1 &\in \mathbb{R}^{n \times M}, [W_1]_{k,l} \sim U \left(\frac{1}{20}, \frac{1}{10} \right) \text{sgn} (U(-1, 1)), \\
\mathbf{W}_2 &\in \mathbb{R}^{n \times n}, [W_2]_{k,l} \sim U \left(\frac{1}{20}, \frac{1}{10} \right) \text{sgn} (U(-1, 1)), \\
\mathbf{W}_4 &\in \mathbb{R}^{n \times n}, [W_4]_{k,l} \sim U \left(\frac{1}{20}, \frac{1}{10} \right) \text{sgn} (U(-1, 1)), \\
\mathbf{b}_1 &\in \mathbb{R}^n, [b_1]_j \sim U \left(-\frac{1}{2}, \frac{1}{2} \right), \\
\mathbf{b}_2 &\in \mathbb{R}^n, [b_2]_j \sim U \left(-\frac{1}{2}, \frac{1}{2} \right), \\
[b_3]_j &= \min_i [x_{2,i}]_j, \\
\mathbf{b}_4 &\in \mathbb{R}^n, [b_4]_j \sim U \left(-\frac{1}{2}, \frac{1}{2} \right).
\end{aligned} \tag{44}$$

This leads to $\mathbf{X} = T_D[\mathbf{Y}] = \{\mathbf{x}_1, \dots, \mathbf{x}_{2500}\}$, where $\mathbf{x}_1 = \frac{1}{4}\mathbf{1}$, with $\mathbf{1} \in \mathbb{R}^n$ having a value of 1 in every component. These points will be part of an continuous 10-dimensional manifold in \mathbb{R}^n .

3. A first function f_1 is then built as

$$f_1(\mathbf{x}) = \min_i \|\mathbf{x} - \mathbf{x}_i\|^2, \tag{45}$$

which has multiple local minima, with $f_1(\mathbf{x}_i) = 0$.

4. A second function f_2 is constructed as

$$f_2(\mathbf{x}) = 3 \left(1 - \exp \left(-10 \|\mathbf{x} - \mathbf{x}_1\|^2 \right) \right) \left(\frac{2}{5} + \exp \left(-10 \|\mathbf{x} - \mathbf{x}_1\|^2 \right) \right), \tag{46}$$

which has one global optimum at \mathbf{x}_1 . Local optimization should lead to the global optimum if initial guesses are within a distance $R = 0.385$ from it (this is the basin X_{\min}).

Local optimization with initial guesses further away will not converge to the global optimum. For 10 000 training samples, the likelihood P_g to randomly sample the global optimum is then:

$$P_g = 1 - (1 - p)^{10000} \approx 0$$

$$\text{for } p = \frac{|X_{\min}|}{|X|} = \frac{\frac{\pi^n}{\Gamma(\frac{n}{2}+1)} R^n}{2^n} = \frac{\frac{\pi^{500}}{\Gamma(501)} 0.385^{1000}}{2^{1000}} \approx 8.3 \times 10^{-1602} \quad (47)$$

5. The final cost function c , with the global minimum at \mathbf{x}_1 , is then given by

$$c_1(\mathbf{x}) = f_1(\mathbf{x}) + f_2(\mathbf{x}). \quad (48)$$

This function is then optimized in two different ways:

- Firstly, the proposed method from § **Methods** is used, with the four steps being implemented as follows:
 1. 10 000 random samples are created by sampling the design space $X = [-1, 1]^n$ uniformly. From these points, the training set \mathbf{X}_{500} is created using Adam with $\alpha = 0.01$, $\beta_1 = 0.9$, and $\beta_2 = 0.999$.
 2. A neural network (see **Fig. 7 A-B**) is then trained with mean squared error loss function for 250 epochs, with the first 225 epochs having 10 batches each, while the last 25 epochs only use one batch. The latent space dimensionality m is chosen as $m = M = 10$, as well as $m = 5$ for a second case.
 3. The optimization over latent space is then performed, using the cost function c_μ (see Equation (5)) with $\mu = 5$. We used differential evolution $\text{DE}_{50,500,0.6,0.9}$ for the optimization of c_1 , and Adam with $\alpha = 0.001$, $\beta_1 = 0.9$, and $\beta_2 = 0.999$ for the local optimization steps LO of c_1 . Here,

$$\text{DE}_{\gamma,G,F,\chi_0} \quad (49)$$

is the notation for setting the hyperparameters of differential evolution (18). These are the population size γ , the number of generations G , the multiplication factor F for the generation of offspring and the probability χ_0 for the crossover operator.

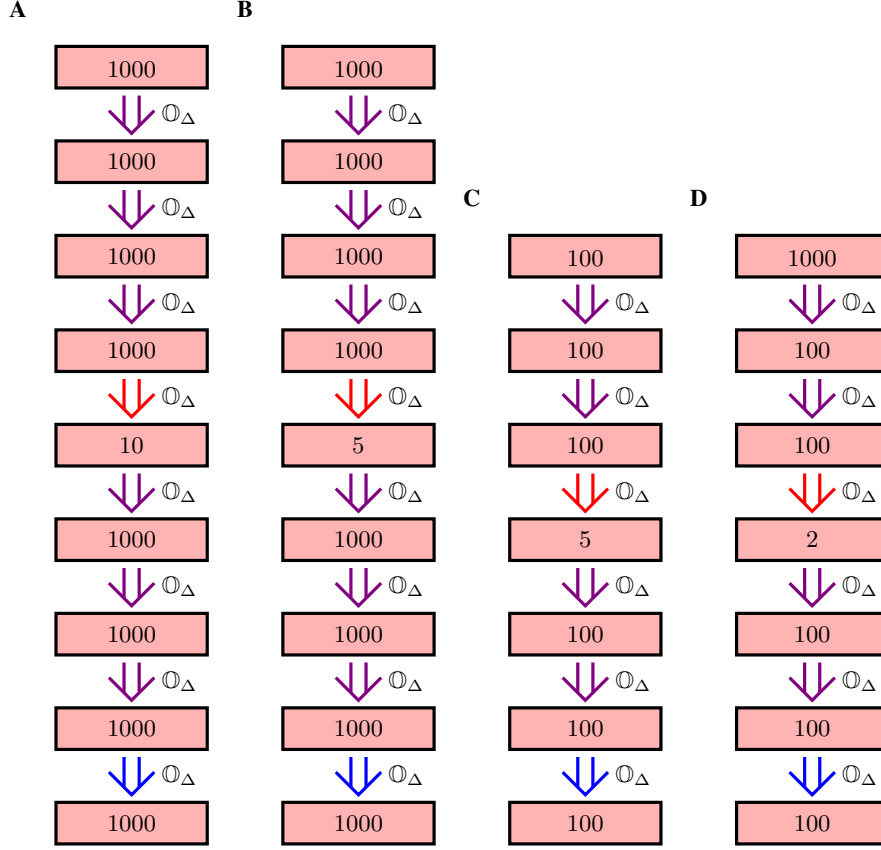


Fig. 7: Neural networks used in sections 2.1 and 2.2 (see **Fig. 10** for symbol explanation). Red arrows indicate the activation function σ_S , blue ones σ_T , and orange ones $\sigma_R \circ \sigma_T$ (see equation (19)). In **A** and **B**, the encoder and decoder used for optimizing c_1 can be seen, with the respective latent space dimensionality ($m \in \{10, 5\}$). On the other hand, in **C** and **D**, the encoder and decoder used for optimizing c_2 , c_3 , and c_4 can be seen, with the respective latent space dimensionality ($m \in \{5, 2\}$).

4. Post-processing consists of $\nu = 1000$ steps, using Adam with $\alpha = 0.001$, $\beta_1 = 0.9$, and $\beta_2 = 0.999$. The post-processing form from equation (7) will be used.

- Alternatively, an optimization over the whole latent space is performed using differential evolution and post processing. Here, during the first steps, $DE_{1000,5000,0.6,0.9}$ is used, while in the post-processing, 500 steps of Adam with $\alpha = 0.001$, $\beta_1 = 0.9$, and $\beta_2 = 0.999$ are performed.

It has to be noted that in **Fig. 2**, the number of function evaluations n_F is a discrete number, but due to the high number of available data points, and to better distinguish between different steps of the process with different types of lines, continuous lines have been used.

2.2 Minimizing c_2 , c_3 , and c_4 from § Benchmark functions

Three benchmark functions from a paper by Abualigah *et al.* (51) were optimized using the method proposed in § **Methods**:

$$\begin{aligned}
 c_2(\mathbf{x}) &= \sum_{i=1}^n \left(-x_i \sin \left(\sqrt{|x_i|} \right) \right) + 418.9829n, \\
 c_3(\mathbf{x}) &= \frac{\pi}{n} \left(10 \sin(\pi y(x_1))^2 + \sum_{i=1}^{n-1} (y(x_i) - 1)^2 \left(1 + 10 \sin(\pi y(x_{i+1}))^2 + u(\mathbf{x}) \right) \right), \\
 y(x) &= \frac{x + 5}{4}, \quad u(\mathbf{x}) = \sum_{i=1}^n 100 \max \{0, |x_i| - 10\}^4, \\
 c_4(\mathbf{x}) &= 1 + \frac{1}{4000} \sum_{i=1}^n (x_i^2) - \prod_{i=1}^n \left(\cos \left(\frac{x_i}{\sqrt{i}} \right) \right).
 \end{aligned} \tag{50}$$

In each case, the original dimension is chosen to be $n = 100$, but with different domains ($X_2 = [-500, 500]^n$, $X_3 = [-50, 50]^n$, $X_4 = [-500, 500]^n$), and latent spaces having a dimension $m = 5$. For all these functions, the minimum cost function value is $c_i = 0$. Each step of the proposed method follows:

- The training set is generated by optimizing $N = 10\,000$ random samples using Adam (parameters in **Tab. 2**) with $\lambda = 125$ steps. However, only half of the samples found (the half with the lower function value) is used for training the neural network; this is done to firstly speed up training, and secondly to avoid training on samples with overall worse fitness.

Tab. 2: Parameters of Adam used for local optimization during the generation of the training set for the optimization of test functions c_2 , c_3 , and c_4 .

c_i	α	β_1	β_2
c_2	30	0.9	0.999
c_3	2.5	0.5	0.75
c_4	20	0.9	0.999

- Before training the autoencoder, the samples are firstly normalized:

$$\mathbf{X}_{\text{train}} = \frac{1}{x_{\text{max}}} \mathbf{X}_\lambda. \tag{51}$$

This is done so that the neural network's output is limited to the domain $[-1, 1]^n$, while $\mathbf{x} \in [-x_{\text{max}}, x_{\text{max}}]^n$. The autoencoders (see **Fig. 7 C-D**) are then trained using Adam for 100 epochs, with 20 batches each, with the mean squared error as the loss function.

- For optimization in latent space, differential evolution $\text{DE}_{5m,2000,0.6,0.9}$ (see equation (49)) was used to optimize c_μ with $\mu = 0$. Decoded samples were renormalized, so that

$$D^*(z) = x_{\max} D(z) \quad (52)$$

was used instead of $D(z)$.

- Finally, during post-processing, Adam was used for $\nu = 2000$ iterations with parameters from **Tab. 3**

Tab. 3: Parameters of Adam used for local optimization during the post-processing for the optimization of test functions c_2 , c_3 , and c_4 .

c_i	α	β_1	β_2
c_2	0.05	0.9	0.999
c_3	0.05	0.9	0.999
c_4	0.5	0.9	0.999

2.3 Compliance minimization

The exact implementation of the four steps of the proposed method (see § **Methods**) for the compliance minimization of a Messerschmitt-Bölkow-Blohm (MBB) beam (see § **Compliance minimization**) is now presented in detail. The optimization problem can be mathematically defined as:

$$\begin{aligned} \mathbf{x}_{\min} &= \underset{\mathbf{x} \in X = [0,1]^{n_y \times n_x}}{\operatorname{argmin}} C(\mathbf{x}) = \mathbf{U}^\top \mathbf{K} \mathbf{U}, \\ \text{subject to: } & \mathbf{K} \mathbf{U} = \mathbf{F}, \\ & \rho(\mathbf{x}) \leq \rho_0, \\ & x_{i,j} = 0 \quad \forall \{i, j\} \in V, \end{aligned} \quad (53)$$

where $\mathbf{K} = \mathbf{K}(\mathbf{x})$ is the stiffness matrix corresponding to the material density field \mathbf{x} , \mathbf{F} is the force vector (shown in **Fig. 3A**), and $\mathbf{U} = \mathbf{U}(\mathbf{x})$ is the displacement degree of freedom vector. Furthermore, $\rho(\mathbf{x})$ (see Equation (9)) and $\rho_0 = 0.4$ are the mean and allowed volume of that design and V is the set of predefined void elements (see white elements in **Fig. 3A**).

Training data set When generating the training set, it is imperative to ensure as wide a variety between samples as possible. And while simply using SIMP to advance to each sample from a random initial density configuration is possible, this approach is not without flaws. Mainly, it is

possible that multiple different starting positions may yield the same result, which would waste computational resources. To avoid this, a method called deflation could be used (56), with the training samples being generated according to the following method:

- 50 initial designs are constructed. The first design $\mathbf{x}_{I,1}$ corresponds to a homogeneous material distribution, while other designs $\mathbf{x}_{I,j}$ ($j \in \{2, \dots, 50\}$) are generated randomly, where $[\mathbf{x}_{I,j}]_k$ is the k -th element of $\mathbf{x}_{I,j}$ and $U(0,1)$ is a value sampled accordingly to the uniform distribution between 0 and 1:

$$[\mathbf{x}_{I,j}]_k = U(0, 1)^{\frac{3}{2}}. \quad (54)$$

- From each initial design $\mathbf{x}_{I,j}$, 100 new designs $\mathbf{x}_{j,a}$ ($a \in \{1, \dots, 100\}$) are created so that each new design is different than previously created ones, using the local optimization step $\text{LO} = \text{SIMP}_{\epsilon, \mathbf{X}_D}$ (see Appendix 1.1):

$$\begin{aligned} \mathbf{x}_{j,a,1} &= \text{SIMP}_{1, \mathbf{X}_{j,a-1,1}}^{25}(\mathbf{x}_{I,j}) \\ \mathbf{x}_{j,a,2} &= \text{SIMP}_{1, \mathbf{X}_{j,a-1,2}}^{225}(\mathbf{x}_{j,a,1}) \\ \mathbf{x}_{j,a} &= \left(\text{SIMP}_{0.25, \emptyset}^{10} \circ \text{SIMP}_{1, \emptyset}^{50} \right) (\mathbf{x}_{j,a,2}) \end{aligned} \quad (55)$$

with $\mathbf{X}_{j,\delta,v} = \{\mathbf{x}_{j,1,v}, \dots, \mathbf{x}_{j,\delta,v}\}$.

This results in 5000 training samples $\mathbf{X}_{300} = \{\mathbf{x}_{j,a} : \forall (j, a) \in \{1, \dots, 50\} \times \{1, \dots, 100\}\}$, from which 4000 are randomly selected to train the autoencoder, while the other 1000 are used for validation of the autoencoder training.

Training the autoencoder After generating the training data set, its samples are used to train an adversarial autoencoder (the discriminator network enforces a uniform distribution over the latent space, with $P_{\text{Dis}} = 1/4$) with a surrogate model network S (with the weight $\beta_S = 1/4$) (for more information see **Fig. 6D** and Appendices 1.3). The specific network architectures used can be seen in **Figs. 8A** and **Figs. 8C**, with a layer architecture mainly chosen based on the results of prior simulations. Additionally, a signed distance field is used to encode the training samples (see Appendix 1.5) with the following weights used in Equation (30) to bias

Furthermore, 50 epochs of pretraining (see Appendix 1.4) are used for the encoder network E and decoder network D , where the first 45 epochs use 10 batches each, and the last 5 epochs only consist of one batch each. During the pretraining, each part of the network is split into $n_{\text{pre}} = 2$ parts, with the outer part consisting of the convolutional layers of the network, and the inner part consisting of the fully connected layers (see **Fig. 8A**). After that, 225 epochs with 10 batches each and further 25 epochs consisting only of one batch are used to train the whole network architecture (see Appendix 1.3).

These settings were used mainly because they yielded superior designs as compared to other network architectures investigated for this problem (see Appendix 2.4). It has to be noted that, to the best of the authors' knowledge, the combination of using a discriminator as well as a surrogate model is novel, the same being true for the use of the signed distance field as a method of encoding the designs.

Optimization over latent space When optimizing over latent space, the cost function

$$c_{\mu}(z) = \left(C \circ \text{SIMP}_{0.25,0}^{10} \circ \text{SIMP}_{1,0}^{\mu} \circ \text{SDF}^{-1} \circ D \right) (z). \quad (57)$$

was optimized with $\mu = 25$. In this equation, as well as in the generation of the training samples, the last part of local optimization using SIMP (this time with a smaller value of ϵ) is done to remove *gray values* (which do not correspond to void nor solid material) from the designs. This is done because, when training samples include gray values, the proposed method will simply prefer designs with larger sparseness during the optimization over latent space, and not designs which are fundamentally different. Therefore, a fair comparison between training samples with gray values and optimized results without would be impossible. Consequently, evaluating if the proposed method indeed let to superior results compared to random multi-start local optimization—or alternatively, if the last three steps of the proposed method are useful—becomes impossible as well. Furthermore, the inclusion of local optimization in the optimization over latent space enforces the mass constraint, which is not always enforced by decoded designs $D(z)$.

In this part, two different methods are applied to optimize the cost function c_{25} :

- Differential evolution $\text{DE}_{300,500,0.6,0.9}$ (see equation (49));

- Bayesian optimization is used, with the main hyperparameters for the method being the number of initial cost function samples evaluated $M_0 = 1000$ and the number of iterations $i_{\text{BO}} = 300$, with each iteration requiring one additional cost function evaluation (see (17)). Differential evolution was applied to fit the surrogate model parameters to the available cost function samples, but the method used differed for each iteration of the Bayesian optimization process. Namely, one used $\text{DE}_{100, G_i, 0.6, 0.9}$ with

$$G_i = \begin{cases} 50 & i \equiv 0 \pmod{100}, \\ 10 & \text{otherwise,} \end{cases} \quad (58)$$

where i is the current iteration of Bayesian optimization. To emphasize exploration of the latent space in the beginning, and exploitation in the end, the following values for ξ_i in the acquisition function EI_i are selected (see (17, 86)):

$$\xi_i = \begin{cases} 10 & i < 200, \\ 0 & i \geq 200. \end{cases} \quad (59)$$

Additionally, the acquisition function EI_i was maximized by minimizing $-\text{EI}_i$ using $\text{DE}_{100, 500, 0.6, 0.9}$.

Post-processing From the optimum z_μ^* , the final design x^* is obtained as

$$x^* = \left(\text{SIMP}_{0.25, \emptyset}^{10} \circ \text{SIMP}_{1, \emptyset}^{300} \circ \text{SDF}^{-1} \circ D \right) \left(z_\mu^* \right). \quad (60)$$

Therefore, the post-processing method given by Equation (7) is used.

2.4 Design variations for compliance minimization

While for the final results an adversarial autoencoder with a surrogate network was used to encode a signed distance field (with $m = 100$ and $\mu = 25$), other possibilities were tested to evaluate which network architecture would lead to the best results; all variations are listed in **Tab. 4**, with the corresponding neural networks shown in **Figs. 8-9**. It has to be noted that, when not using the signed distance field but the density to encode the designs, the following weights were used in Equation (30):

$$w_j = 2(1 - |x_j - 0.5|). \quad (61)$$

Each of these variations, all using the same training data, are then executed four times to take into account the randomness in initializing the neural network parameters (see Appendix 1.3)

and the optimization over latent space (only differential evolution was used due to speed, see Appendix 3.6).

The method is then deemed to be successful if it can reliably produce final results whose compliance value C is lower than the lowest compliance obtained from the training samples. From the 64 different tested variations, this was achieved in 14 cases. Some variations were more successful than others (see **Tab. 5**), with a 100-dimensional latent space, and using pre-training, a discriminator, encoding a signed distance field, and using $\mu = 25$ steps of local optimization having the best results. The superiority of adding the discriminator (which transforms an autoencoder into an adversarial autoencoder) agrees with the result of Kudyshev *et al.* (43), i.e., the choices made and adding a surrogate model lead to the least compliant result and the lowest compliance when averaged over all four tries.

The fact that 30 of the test cases were never able to outperform the training set shows that even if the underlying assumption about the cost function seems to be true—as shown by the superior results that could be achieved—one still needs to be careful when constructing the network used to extract the features of the useful parts of the design space.

3 Supplementary text

3.1 Intrinsic dimensionality of an optimization problem

We try to construct an autoencoder with a decoder $D_\theta : \mathbb{R}^m \rightarrow \mathbb{R}^n$, which is parameterized with the weights and biases $\theta \in \Theta$, which allows to construct a decoded latent space $X_Z(\theta)$, optimizing over which enables us to find the global optimum \mathbf{x}_{\min} . For this to be possible, $\theta \in \Theta^*$ is necessary, with

$$\Theta^* = \{\theta : X_Z(\theta) \cap X_{\min} \neq \emptyset\} \subset \Theta, \quad (62)$$

where X_{\min} is the basin of \mathbf{x}_{\min} , i.e.,

$$X_{\min} = \left\{ \mathbf{x} : \lim_{\nu \rightarrow \infty} (\text{LO}^\nu(\mathbf{x})) = \mathbf{x}_{\min} \right\} \subset X. \quad (63)$$

Here it has to be mentioned that theoretically one could also use $\Theta^* = \{\theta : \mathbf{x}_{\min} \in X_Z(\theta)\}$, but due to the inclusion of local optimization steps during the optimization over latent space and the use of post-processing (see § **Methods**), the softer criterion given by (62) can be used.

Before training the autoencoder, an initial θ has to be chosen according to a prior probability distribution $p_0(\theta)$. During training then, these parameters are changed according to the autoencoder loss function \mathcal{L} and the training samples $\mathbf{X} = \{\mathbf{x}_i \sim p_{\mathbf{X}}(\mathbf{x}) : i = \{1, \dots, N\}\}$, resulting in the posterior $p(\theta)$ (which depends on $p_0(\theta)$, $p_{\mathbf{X}}$ and \mathcal{L} as well as the training algorithm used). This posterior would also theoretically allow the calculation of $p_{X_Z}(\mathbf{x})$

$$p_{X_Z}(\mathbf{x}) = P(\mathbf{x} \in X_Z) = \int_{\{\theta: \mathbf{x} \in X_Z(\theta)\}} p(\theta) d\theta \quad (64)$$

One can then calculate the probability of a successful optimization run P^* in two ways:

$$\begin{aligned} P^* &= P(\theta \in \Theta^*) = \int_{\Theta^*} p(\theta) d\theta \\ &= P(X_Z \cap X_{\min} \neq \emptyset) = \int_{X_{\min}} p_{X_Z}(\mathbf{x}) d\mathbf{x} \end{aligned} \quad (65)$$

This probability $P^*(m)$ depends on the latent space dimensionality m , and it can be assumed that it will grow with it, as expanding m will likely grow Θ^* . Consequently, for a given set minimum probability P_{\min} where we see the likelihood of successfully finding the global minimum as sufficiently high, one can find the intrinsic dimensionality m^* of the optimization problem considered as

$$m^* = \min \{m : P^*(m) > P_{\min}\}, \quad (66)$$

It has to be noted that besides m , P^* will also depend on other variables, namely $p_0(\theta)$, $p_{\mathbf{X}}$, \mathcal{L} , and the autoencoder training algorithm. Our assumption that now underlies our proposed method is that $m^* \ll n$.

It has to be noted that, while P_{\min} is inherently subjective, an objective lower bound can be given when comparing the proposed method to another global optimization algorithm. For the proposed method, this would be $P_{\min}^{-1} t_{\text{PM}}$ (see Appendix 3.2), where t_{PM} is the time required for one run of our proposed method, while t_{GO} is the average time needed for the compared algorithm to find the global optimum. Then

$$P_{\min} > \frac{t_{\text{PM}}}{t_{\text{GO}}}. \quad (67)$$

Secondly, it is also important to note that P^* is only an upper bound to the real-world probability of finding the global optimum, since it assumes that the global optimization algorithm used for surveying the latent space is capable of always finding $\mathbf{z}_{\mu \rightarrow \infty}^*$ (see Equation (5)); this would

require a brute force minimization of $c_{\mu \rightarrow \infty}$, which is impossible with limited computational resources. Firstly, we can not optimize c_μ with $\mu \rightarrow \infty$, but have to use instead a limited number of local optimization steps μ . Secondly, we cannot use brute force over the continuous domain Z , and therefore have to use an optimization algorithm that can become trapped in a local minimum of c_μ . The real-world probability of finding the global optimum is hence likely somewhat lower than P^* .

3.2 On the average number of tries until success

The average number a of tries necessary to get an event with a single instance likelihood of p has to be calculated. We can define the probability $P(a)$ that an event will not happen $a - 1$ consecutive times and then happen on the a th try as

$$P(a) = p(1 - p)^{a-1}. \quad (68)$$

The average number of tries a^* is then:

$$\begin{aligned} a^* &= \sum_{a=1}^{\infty} aP(a) \\ &= \sum_{a=1}^{\infty} ap(1 - p)^{a-1} \\ &= \frac{p}{1 - p} \sum_{a=1}^{\infty} a(1 - p)^a \\ &= \frac{p}{1 - p} \frac{1 - p}{((1 - p) - 1)^2} \\ &= \frac{1}{p}. \end{aligned} \quad (69)$$

For the second to last step, see the Li_{-1} polylogarithm.

3.3 Intrinsic dimensionality of c_1 from § Benchmark functions

In this problem, the cost function is designed so that it has its local minima aligned on a 10-dimensional domain inside the higher-dimensional search space X . This makes it likely that the probability distribution p_X of the training sample will be high around these points and lower elsewhere. If the autoencoder's latent space dimensionality m now matches—or surpasses—the dimensionality of the manifold containing the local minima and the autoencoder training is successful, then one should see (with ς as scaling factor):

$$p_{X_Z} \approx \varsigma p_X. \quad (70)$$

Based on this, one can then calculate the likelihood P^* of including the decoded latent space in the basin of the global optimum:

$$P^* = P(X_Z \cap X_{\min} \neq \emptyset) = \int_{X_{\min}} p_{X_Z}(\mathbf{x}) \, d\mathbf{x} \approx \int_{X_{\min}} \varsigma p_X(\mathbf{x}) \, d\mathbf{x}. \quad (71)$$

As p_X is high around all local minima and therefore also around the global optimum, it can be assumed that P^* will be high enough for $m = 10$, which makes the intrinsic dimensionality of the problem $m^* = 10$ (see Appendix 3.1).

3.4 Results for c_3 and c_4 from § Benchmark functions

In § **Benchmark functions** we observed the tendency of autoencoders encoding evenly spread samples \mathbf{X} from an n -dimensional manifold onto an m -dimensional latent space Z to include the mean of the samples $\bar{\mathbf{x}}$ in the decoded latent space X_Z . **This can** It can likely be explained by the fact that the mean has the lowest reconstruction error of any point when encoding a random cluster into a single point, which incentivizes the autoencoder to include this point in its decoded latent space X_Z :

$$\bar{\mathbf{x}} = \operatorname{argmin}_{\mathbf{x} \in X} \sum_i \|\mathbf{x}_i - \mathbf{x}\|^2 \quad (72)$$

This can be proven by firstly considering a one-dimensional problem:

$$\begin{aligned} \sum_i (x_i - x)^2 &= \sum_i (x_i^2 - 2x_i x + x^2) \\ &= \sum_i (x_i^2) - 2x \sum_i (x_i) + nx^2 \\ &= \sum_i (x_i^2) - n\bar{x}^2 + n\bar{x}^2 - 2nx\bar{x} + nx^2 \\ &= \sum_i (x_i^2) - n\bar{x}^2 + n(x - \bar{x})^2 \\ &= n(x - \bar{x})^2 + c \end{aligned} \quad (73)$$

$$\begin{aligned} \operatorname{argmin}_x \sum_i (x_i - x)^2 &= \operatorname{argmin}_x n(x - \bar{x})^2 + c = \bar{x} \\ \operatorname{argmin}_x \sum_i \|\mathbf{x}_i - \mathbf{x}\|^2 &= \operatorname{argmin}_x \sum_{j=1}^n \sum_i \|[x_i]_j - [x]_j\|^2 = \bar{\mathbf{x}}. \end{aligned} \quad (74)$$

When setting this into the probabilistic terms in Appendix 3.1, it could be assumed here for a thoroughly trained autoencoder that

$$p_{X_Z}(\mathbf{x}) \approx \frac{\varsigma_1}{\|\bar{\mathbf{x}} - \mathbf{x}\|^{n-m}}, \quad (75)$$

where ς_1 is a scaling constant. From this, it is clear that the likelihood for successful optimization

$$P^* = P(X_Z \cap X_{\min} \neq \emptyset) = \int_{X_{\min}} p_{X_Z}(\mathbf{x}) \, d\mathbf{x} \approx \frac{\varsigma_2}{\|\bar{\mathbf{x}} - \mathbf{x}\|^{n-m}}. \quad (76)$$

is high for a global minimum close to the center $\bar{\mathbf{x}}$, and consequently $m^* \ll n$ in this cases, with m^* being lower the larger X_{\min} is in relation to the search space X . But on the other hand, P^* is rapidly decreasing when the global optimum moves away from the center. Consequently, in most cases, where $\bar{\mathbf{x}} \not\approx \mathbf{x}_{\min}$ and p_X is approximately uniform (the means regular distribution of local minima in X), one can find $m^* = n$.

3.5 On the size of the design space in § Compliance minimization

In the compliance minimization problem we use a mesh of $n_y \times n_x = 45 \times 90$ quadrilateral elements and a set of 154 enforced void elements, *i.e.*, $|V| = 154$. Due to the penalization of intermediate density values in SIMP, the optimal design has to be sparse, which means the density of every element $x_j \in \{0, 1\}, \forall x_j \in \mathbf{x}_s, \forall \mathbf{X}_s \in X_s$. Consequently, there are $|X_s| = 2^{n_y n_x - |V|} = 2^{3896} \approx 6.5 \times 10^{1172}$ possibly optimal designs. This set is further restricted by the mass constraint, which provides a maximum number $\rho_0 n_y n_x = 1620$ of elements that can have $x_j = 1$. As removing material from a design—or equivalently reducing the density and therefore the Young’s modulus of certain mesh elements—will only weaken a design and therefore make it more compliant, it can also be assumed that the optimal design will use as much material as possible. Consequently, the number of possibly optimal designs which fulfill the constraint is equal to the number of possibilities to choose 1620 instances from a set including 3896 possible choices:

$$\binom{3896}{1620} \approx 6.7 \times 10^{1146}. \quad (77)$$

3.6 Evaluation time for the optimization over latent space for § Compliance minimization

When trying to approximate the running time for optimization over latent space, there are three variables to consider. The first two variables are the cost function evaluation time t_c and the time needed for modeling in Bayesian optimization t_M , both measured when running on a single processor core. The third variable is the number of available processes N_p . For the implementation

used (see Appendix 2.3), we can calculate t_{DE} and t_{BO} (overhead of parallelization is neglected here):

$$\begin{aligned} t_{\text{DE}} &= G \left\lceil \frac{\gamma}{N_p} \right\rceil t_c = 500 \left\lceil \frac{300}{N_p} \right\rceil t_c, \\ t_{\text{BO}} &= \left(\left\lceil \frac{M_0}{N_p} \right\rceil + i_{\text{BO}} \right) t_c + \frac{t_M}{N_p} = \left(\left\lceil \frac{1000}{N_p} \right\rceil + 300 \right) t_c + \frac{5000000\text{sec}}{N_p}. \end{aligned} \quad (78)$$

When considering the viability of using Bayesian optimization, two factors are important. The first one is $t_{c,0}$, the point after which Bayesian optimization becomes more efficient:

$$\begin{aligned} t_c \geq t_{c,0} &\iff t_{\text{DE}} \geq t_{\text{BO}} \\ \Rightarrow t_c = t_{c,0} &\iff t_{\text{DE}} = t_{\text{BO}} \\ G \left\lceil \frac{\gamma}{N_p} \right\rceil t_{c,0} &= \left(\left\lceil \frac{M_0}{N_p} \right\rceil + i_{\text{BO}} \right) t_{c,0} + \frac{t_M}{N_p} \\ t_{c,0} &= \frac{t_M}{G(\gamma - \gamma \bmod N_p) - (M_0 - M_0 \bmod N_p) - N_p i_{\text{BO}}} \\ t_{c,0} &= \frac{5000000\text{sec}}{500(300 - 300 \bmod N_p) - (1000 - 1000 \bmod N_p) - 300N_p}. \end{aligned} \quad (79)$$

For $t_{c,0} > 0$, the other important information is then the factor k_t , which describes how much better using:

$$k_t = \left. \frac{t_{\text{DE}}}{t_{\text{BO}}} \right|_{t_c \rightarrow \infty} = \frac{G \left\lceil \frac{\gamma}{N_p} \right\rceil}{\left\lceil \frac{M_0}{N_p} \right\rceil + i_{\text{BO}}} = \frac{500 \left\lceil \frac{300}{N_p} \right\rceil}{\left\lceil \frac{1000}{N_p} \right\rceil + i_{\text{BO}}}. \quad (80)$$

For $N_p = 100$, as used in this work, then $t_{c,0} \approx 42.0s$ and $k_t \approx 4.84$. If no parallelization is possible ($N_p = 1$), then $t_{c,0} \approx 33.6s$ and $k_t \approx 115.4$. If there exists an efficient parallelization of the cost function itself, with a negligible overhead, then the problem becomes similar to $N_p = 1$ in every case. While the equations used here are general, it has to be noted that the final values are only valid for this specific case.

3.7 On the need for post-processing

It can be assumed that the result z^* of the third step of the proposed method will be a local optimum of c_μ in latent space. But the decoded sample $\chi_\mu(z^*)$ would not necessarily correspond to a local minimum of c . Mathematically,

$$\begin{aligned} \left. \frac{\partial c_\mu(z)}{\partial z} \right|_{z=z^*} &= \left. \frac{\partial c(\chi_\mu(z))}{\partial z} \right|_{z=z^*} = \left. \frac{\partial c(\mathbf{x})}{\partial \mathbf{x}} \right|_{\mathbf{x}=\chi_\mu(z^*)} \left. \frac{\partial \chi_\mu(z)}{\partial z} \right|_{z=z^*} = \mathbf{0} \\ &\not\equiv \left. \frac{\partial c(\mathbf{x})}{\partial \mathbf{x}} \right|_{\mathbf{x}=\chi_\mu(z^*)} = \mathbf{0}. \end{aligned} \quad (81)$$

For easier notation,

$$\left. \frac{\partial c(\mathbf{x})}{\partial \mathbf{x}} \right|_{\mathbf{x}=\chi_\mu(z^*)} = \mathbf{b} \in \mathbb{R}^{1 \times n} \quad (82)$$

and

$$\left. \frac{\partial \chi_\mu(z)}{\partial z} \right|_{z=z^*} = \mathbf{A} \in \mathbb{R}^{n \times m} \quad (83)$$

are defined. One then can proof equation (81) by recognizing $\mathbf{bA} = \mathbf{0}$ as a homogeneous system of linear equations—*i. e.*, it is consistent and the trivial solution $\mathbf{b} = \mathbf{0}$ will always work. But for $m < n$, $\mathbf{bA} = \mathbf{0}$ is an underdetermined system of linear equations, which means that an infinite number of other solutions exist for this problem besides $\mathbf{b} = \mathbf{0}$. Consequently, the claim $\mathbf{bA} = \mathbf{0} \Rightarrow \mathbf{b} = \mathbf{0}$ is indeed incorrect.

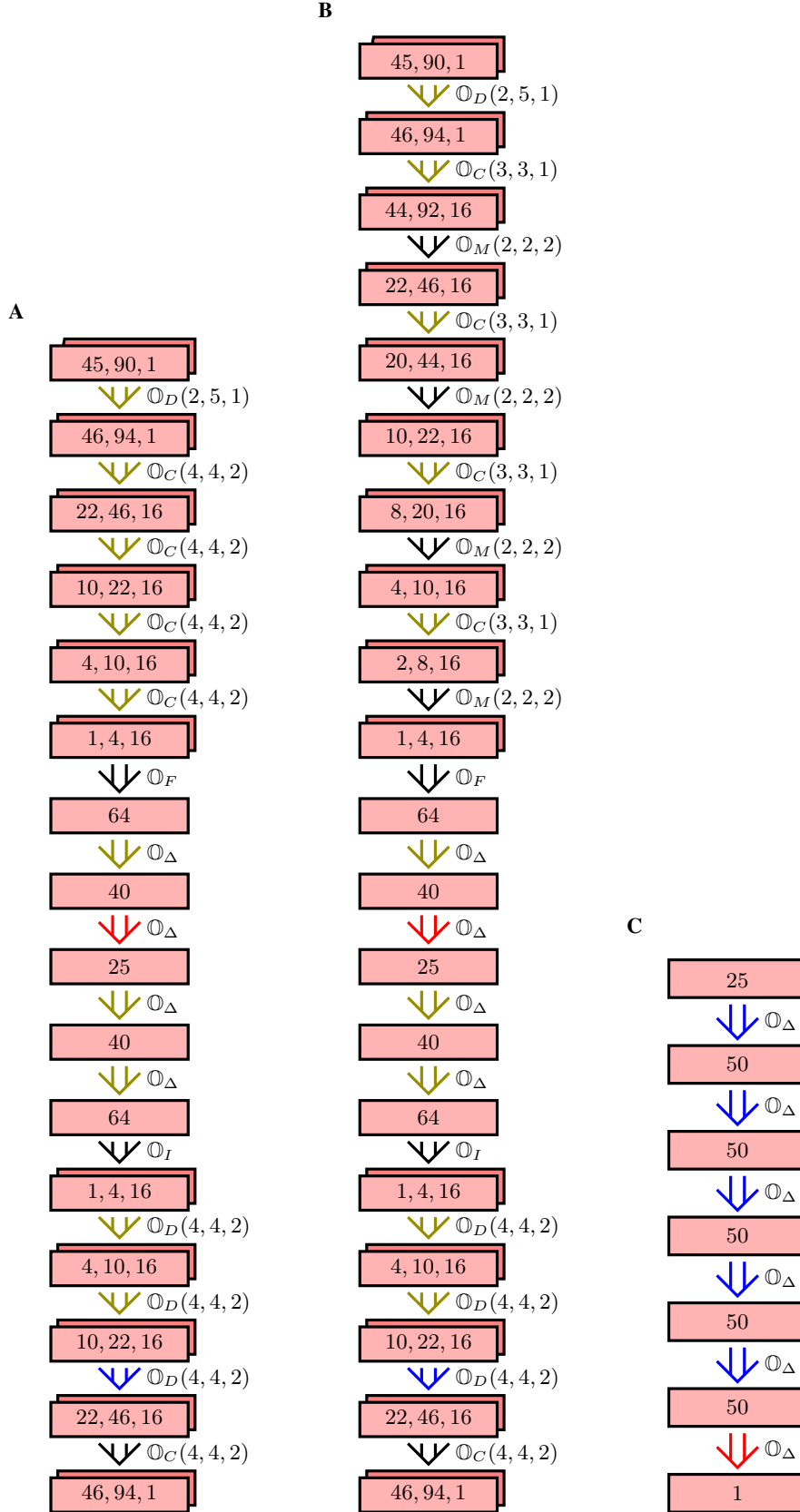


Fig. 9: Neural networks used in section 2.3 (see **Fig. 10** for symbol explanation). Red arrows indicate the activation function σ_S , blue ones σ_T , olive ones σ_R , and black ones σ_I (see equation (19)). In **A** and **B**, the encoder and decoder for the case $m = 25$ can be seen, respectively for encoding a signed distance or a density field. In **C**, one can then see the discriminator and surrogate model network for $m = 25$, which have the same architecture.

Tab. 4: The different variations of autoencoder enabled global optimization tested for the compliance minimization problem. Variation δ_1 is the number of latent space dimensions m , δ_{2-4} varies the use of certain techniques and network architectures, variation δ_5 is the encoding method, and the last varied point is the number of local optimization steps during optimization over latent space μ .

i	$\delta_i = 0$	$\delta_i = 1$
1	$m = 25$	$m = 100$
2	w/o pret.	w/ pret.
3	w/o D_{Dis}	w/ D_{Dis}
4	w/o S	w/ S
5	Density field	SDF
6	$\mu = 1$	$\mu = 25$

Tab. 5: The ratio of successful variations of autoencoder enabled global optimization (see **Tab. 4**) for the compliance minimization problem, given in percent.

i	$\delta_i = 0$	$\delta_i = 1$
1	28.6	71.4
2	21.4	78.6
3	35.7	64.3
4	50.0	50.0
5	35.7	64.3
6	0	100

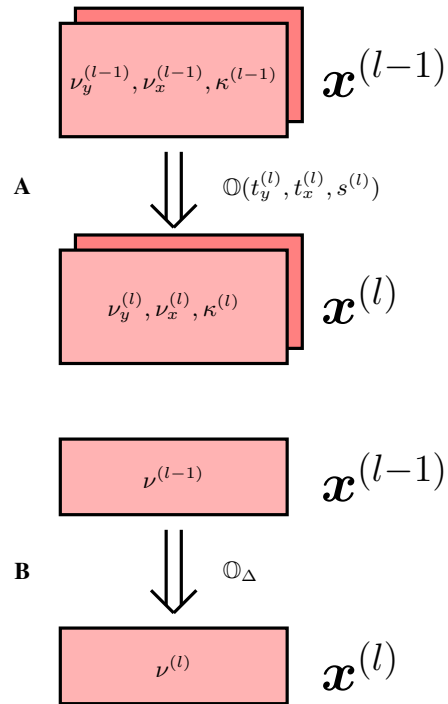


Fig. 10: Symbolic representation of different connections from layer $\mathbf{x}^{(l-1)}$ to $\mathbf{x}^{(l)}$. In **A**, the depiction is of either convolutional ($\mathbb{O} = \mathbb{O}_C$), max pooling ($\mathbb{O} = \mathbb{O}_M$), or deconvolutional ($\mathbb{O} = \mathbb{O}_D$) connections. In **B**, the depiction is of a dense connection, marked with \mathbb{O}_Δ . The activation function used will be marked by the color of the arrow connecting the different layers.